A DGTD method for the numerical modeling of the interaction of light with nanometer scale metallic structures taking into account non-local dispersion effects

Nikolai Schmitt, Claire Scheid, Stéphane Lanteri, Jonathan Viquerat, Antoine Moreau

A DGTD method for the numerical modeling of the interaction of light with nanometer scale metallic structures taking into account non-local dispersion effects

Nikolai Schmitt, Claire Scheid, Stéphane Lanteri, Jonathan Viquerat, Antoine Moreau

RESEARCH REPORT

N° 8726

May 2015

Project-Team Nachos

ISSN 0249-6399 ISRN INRIA/RR--8726--FR+ENG

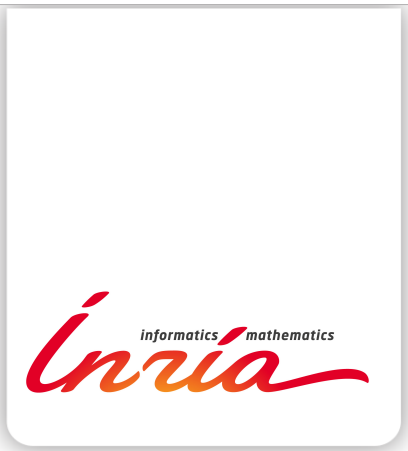

A DGTD method for the numerical modeling of the interaction of light with nanometer scale metallic structures taking into account non-local dispersion effects

Nikolai Schmitt*, Claire Scheid†, Stéphane Lanteri, Jonathan Viquerat‡, Antoine Moreau§

Project-Team Nachos

Research Report n° 8726 — May 2015 — 73 pages

* Technische Universität Darmstadt, Institut für Theorie Elektromagnetischer Felder, Schlobgartenstr. 8, 64289 Darmstadt, Germany

† University of Nice - Sophia Antipolis, Mathematics laboratory, Parc Valrose, 06108 Nice, Cedex 02, France

‡ Inria, 2004 Route des Lucioles, BP 93 06902 Sophia Antipolis Cedex, France

§ Institut Pascal, Université Blaise Pascal, 24, avenue des Landais, 63171 Aubière Cedex, France

RESEARCH CENTRE
SOPHIA ANTIPOLIS – MÉDITERRANÉE

2004 route des Lucioles - BP 93

06902 Sophia Antipolis Cedex

Abstract: The interaction of light with metallic nanostructures is of increasing interest for various fields of research. When metallic structures have sub-wavelength sizes and the illuminating frequencies are in the regime of metal's plasma frequency, electron interaction with the exciting fields have to be taken into account. Due to these interactions, plasmonic surface waves can be excited and cause extreme local field enhancements (e.g. surface plasmon polariton electromagnetic waves). Exploiting such field enhancements in applications of interest requires a detailed knowledge about the occurring fields which can generally not be obtained analytically. For the latter mentioned reason, numerical tools as well as a deeper understanding of the underlying physics, are absolutely necessary. For the numerical modeling of light/-structure interaction on the nanoscale, the choice of an appropriate material model is a crucial point. Approaches that are adopted in a first instance are based on local (i.e. with no interaction between electrons) dispersive models e.g. Drude or Drude-Lorentz models. From the mathematical point of view, when a time-domain modeling is considered, these models lead to an additional system of ordinary differential equation which is coupled to Maxwell's equations. When it comes to very small structures in a regime of 2 nm to 25 nm, non-local effects due to electron collisions have to be taken into account. Non-locality leads to additional, in general non-linear, system of partial differential equations and is significantly more difficult to treat, though. Nevertheless, dealing with a linear non-local dispersion model is already a setting that opens the route to numerous practical applications of plasmonics. In this work, we present a Discontinuous Galerkin Time-Domain (DGTD) method able to solve the system of Maxwell equations coupled to a linearized non-local dispersion model relevant to plasmonics. While the method is presented in the general 3d case, numerical results are given for 2d simulation settings only.

Key-words: Maxwell's equations, time-domain, discontinuous Galerkin, non-local dispersion, hydrodynamic Drude model, nanophotonics, plasmonics

Une méthode Galerkin discontinue en domaine temporel pour la modélisation numérique de l'interaction lumière/structure métallique aux échelles nanométriques en présence d'effets dispersifs non-locaux

Résumé : L'interaction lumière/nanostructures métalliques est d'intérêt croissant pour plusieurs domaines de la recherche. Lorsque les structures métalliques ont des tailles plus petites que la longueur d'onde et les fréquences d'illumination sont proches de la fréquence plasma, les phénomènes liés aux interactions entre électrons et champs incidents doivent être pris en compte avec des modèles comportementaux appropriés. Du fait de ces interactions, des ondes plasmoniques surfaciques peuvent être excitées et conduire à des exaltations locales du champ. L'exploitation de ces phénomènes d'exaltation dans les applications d'intérêt nécessite une connaissance détaillée du comportement des champs qui ne peut généralement pas être obtenue analytiquement. Pour cete raison, le recours à la modélisation numérique s'impose presque toujours. Pour la modélisation numérique de l'interaction lumière/matière aux échelles nanométriques, la sélection d'un modèle comportemental du milieu approprié est une étape cruciale. Une approche souvent considérée en première instance consiste à adopter un modèle dispersif local tel que le modèle de Drude ou le modèle de Drude-Lorentz. Ces modèles se traduisent par la prise en compte d'équations différentielles ordinaires qui sont couplées aux équations de Maxwell instationnaires. Cependant, lorsque la taille des nanostructures diminue dans l'intervalle 2 nm à 25 nm, des effets dispersifs non-locaux doivent être pris en compte. La non-localité se matérialise par un système d'équations aux dérivées partielles possiblement non-linéaires qui s'ajoute aux équations de Maxwell. Dans cette étude, nous présentons une méthode de type Galerkin discontinu en domnaine temporel pour la résolution numérique des équations de Maxwell 2d couplées à un modèle de dispersion non-local linéarisé pour des applications en nanoplasmonique.

Mots-clés : équations de Maxwell, domaine temporel, Galerkin discontinu, dispersion non-locale, modèle de Drude hydrodynamique, nanophotonique, plasmonique.

Contents

List of Figures

List of Tables

1 Motivations and goals

1.1 Physical background

Nanometer scale (or even sub-nanometer scale) metallic or metallo-dielectric devices enlightened at optical frequencies demonstrate interesting features that are increasingly exploited in the area of nanophotonics. To be able to optimize the use of these enhanced properties, an appropriate modeling is required, in particular, to describe the reaction of the electrons in the metal subjected to an incident electromagnetic wave as precisely as possible. At the scales and frequencies considered in this context, the classical description of the propagation of an electromagnetic wave is not enough and the electric dispersion of the metal has to be taken into account. First, the electrons do not react instantaneously to the applied electric field. Furthermore, at sub-nanometer scales, it appears that quantum effects must be taken into account: the electron behavior not only depends on the field at the position of the electron (*local response*) but also on the neighboring field distribution (*non-local response*). These dispersion effects manifest as the existence of a polarization of the electron. The latter enters the modeling in the form of a polarization current in the system of Maxwell equations. The space-time evolution of this polarization current is governed by a set of differential equations which is itself linearly coupled to the classical set of Maxwell equations. If one chooses to neglect non-local effects and thus consider a local dispersion model, the additional equations form a system of ordinary differential equations. This type of model can yield a good description of the dispersion effects in metals if the scales are not too small. But at very small scales, one has to consider a non-local response of the electrons in the model [1]. In this case, the equations governing the evolution of the polarization current are partial differential equations. This type of model is at the heart of the study proposed here.

1.2 Numerical modeling issues

In the area of computational nanophotonics, there is currently a need for efficient and accurate numerical methodologies since the geometries, scales and propagation media can be rather complex. In the literature, a large number of studies are devoted to FDTD (Finite Difference Time-Domain) type discretization methods based on Yee's scheme. Despite their numerous advantages (efficiency and easy implementation), these FDTD methods poorly perform when facing the modeling difficulties that are inherent to nanophotonic applications, in particular in the presence of curved geometries. Indeed, the stair-casing effect resulting from the use of a cartesian grid notably degrades the accuracy of these FDTD methods. Numerical methods based on unstructured and possibly non-conforming meshes[1] are particularly appealing in this context. This is especially the case for approaches based on

[1] The term *non-conforming meshes* is used by means of meshes with hanging nodes.

a Discontinuous Galerkin (DG) formulation. So-called DGTD (Discontinous Galerkin Time-Domain) methods mix the best of finite element and finite volume type discretization methods, and are based on a local formulation on each elements of the mesh, while the continuity constraint at the element boundaries is relaxed, thus requiring an appropriate treatment of inter-element boundary integrals appearing in the weak formulation. The latter leads to the definition of a numerical trace or numerical flux (in the spirit of finite volume schemes). These DGTD methods are possibly high order and are flexible enough to deal with heterogeneous media and complex geometries. They are especially well-suited to parallel computations, therefore reducing the computational costs when simulating three-dimensional problems. Their use in the nanophotonic area is still limited but one can notice a growing interest in this direction (see e.g. [2]-[3]). Noteworthy, all these studies adopt a diffusive DGTD formulation based on upwind numerical fluxes. Besides, several studies have already been conducted regarding the development of DGTD methods for dispersive media, such as, [4], [5]. Furthermore one can find more studies focused on numerical analysis aspects concerning dispersive media [6]-[7]. In the framework of non-dissipative formulations [8], a DGTD method able to treat local dispersive models for metallic structures has recently been designed and studied in [9].

1.3 Objectives of this study and related works

The present work is concerned with the design and numerical study of a DGTD method for solving the system of time-domain Maxwell equations coupled to a linearized fluid model that governs the non-local dispersive behavior of metals. The problem statement in the three-dimensional (3d) case and the corresponding initial and boundary value problem are described in section 2. As in [8]-[9], the proposed DGTD formulation combines a centered numerical flux with a second order leap-frog time integration scheme. This is detailed in section 3. From the theoretical viewpoint, we conduct a stability analysis of the resulting DGTD method and show that the method is stable under a CFL condition. Finally, this DGTD method is implemented in the two-dimensional (2d) case for the transversal electric mode formulation of Maxwell's equations and some validation test problems are presented. This is the subject of section 5.

2 Problem statement and notations

This section introduces the underlying physics and models that will be numerically solved later. Beginning with Maxwell's macroscopic equations for electrodynamics, the Drude dispersion model is presented afterwards. In order to improve the modeling quality and taking interband effects into account, the Drude-Lorentz model is briefly motivated. Since these dispersion models do not consider any electron

interactions they remain absolutely local. For a certain dimensional range of nano-photonic devices, non-local effects in terms of electron interactions have to be taken into account. If those dimensions become even smaller down to a level where the quantum mechanics (QM) behavior of electrons, i.e. tunneling through regions that are classically forbidden occur, even semi-classical non-local models are not sufficient anymore and full QM descriptions are required. In this work, we will not consider dimensions where the latter descriptions are necessary and though stick to effects that can be sufficiently modeled with a so called non-local hydrodynamic fluid model.

As this work is mainly concerned with non-local dispersion models, the local dispersion effects are kept shortly while focusing on the physics which cause the non-local dispersion of metals in a frequency regime around and beyond the plasma frequency. Then, the hydrodynamic modeling that governs the electron coupling is presented and we derive the linearized fluid model from a general non-linear hydrodynamic model. Maxwell's equations together with the latter mentioned linearized fluid model lead to a new system of partial differential equations (PDEs). In order to characterize this PDE system, we show its hyperbolicity and analyze the energy evolution in time. As the numerical treatment is here restricted to the 2d case (in a sense of an invariance in one given direction), it appears that non-local effects do only occur in the so called TE (transverse electric) mode and thus the TM (transverse magnetic) mode can be left out. This section closes with a proper definition of the here considered boundary value problem and a comparison of the local and non-local models. Additionally, a renormalized form of the model problem is derived for the purpose of the implementation.

2.1 The system of Maxwell equations

The complete set of macroscopic Maxwell's equations describing the spatio-temporal evolution of electromagnetic waves are given by (see for example [10])

$$\int_{\partial \mathrm{A}} \mathbf{E}(\mathbf{r},t)\cdot \mathrm{d}\mathbf{s} = -\int_{\mathrm{A}} \partial_t \mathbf{B}(\mathbf{r},t)\cdot \mathrm{d}\mathbf{A}, \tag{1a}$$

$$\int_{\partial \mathrm{A}} \mathbf{H}(\mathbf{r},t)\cdot \mathrm{d}\mathbf{s} = \int_{\mathrm{A}} \left(\partial_t \mathbf{D}(\mathbf{r},t) + \mathbf{J}(\mathbf{r},t)\right)\cdot \mathrm{d}\mathbf{A}, \tag{1b}$$

$$\int_{\partial \mathrm{V}} \mathbf{D}(\mathbf{r},t)\cdot \mathrm{d}\mathbf{A} = \int_{\mathrm{V}} \rho \, \mathrm{d}V, \tag{1c}$$

$$\int_{\partial \mathrm{V}} \mathbf{B}(\mathbf{r},t)\cdot \mathrm{d}\mathbf{A} = 0, \tag{1d}$$

with

$$
\begin{aligned}
&\Omega : \text{3d domain},\\
&\partial\Omega : \text{boundary of } \Omega,\\
&\mathrm{V} : \mathrm{V} \subset \Omega, \quad \mathrm{A} := \partial \mathrm{V},\\
&\partial_t : \text{partial time derivative with respect to } t,\\
&\mathbf{a} \cdot \mathbf{b} : \text{scalar product of } \mathbf{a} \text{ and } \mathbf{b},\\
&\mathbf{r} \in \mathbb{R}^3, \quad t \in \mathbb{R}^+,\\
&\mathbf{E}, \mathbf{D}, \mathbf{H}, \mathbf{B}, \mathbf{J} : \mathbb{R}^3 \times \mathbb{R} \mapsto \mathbb{R}^3,\\
&\rho : \mathbb{R}^3 \times \mathbb{R} \mapsto \mathbb{R}.
\end{aligned}
\tag{2}
$$

Here, $\mathbf{E}$ and $\mathbf{H}$ represent the electric and magnetic field, respectively. The magnetic flux density is denoted by $\mathbf{B}$ as well as the electric displacement and current density by $\mathbf{D}$ and $\mathbf{J}$, respectively and the charge density by ρ. The infinitesimal spatial elements $\mathrm{d}\mathbf{s}, \mathrm{d}\mathbf{A}$, and $\mathrm{d}V$ represent the vectorial line element, the vectorial surface element where the normal vector points outwards the volume V and the volume element, respectively. As Maxwell's equations are a set of equations that were individually discovered before (without the electric displacement), they are commonly known as Faraday's law, Ampère's law, Gauss's law and the absence of magnetic monopoles for (1a), (1b), (1c), (1d), respectively [10]. Applying Stokes' theorem to (1a) and (1b) and the theorem of Gauss to (1c) and (1d), (1) can be written in differential form

$$\nabla \times \mathbf{E} = -\partial_t \mathbf{B}, \tag{3a}$$

$$\nabla \times \mathbf{H} = \partial_t \mathbf{D} + \mathbf{J}, \tag{3b}$$

$$\nabla \cdot \mathbf{D} = \rho, \tag{3c}$$

$$\nabla \cdot \mathbf{B} = 0, \tag{3d}$$

where $\nabla \times \mathbf{A}$, and $\nabla \cdot \mathbf{A}$ denote the curl and the div operator applied to a quantity $\mathbf{A}$. These equations are supplemented by material laws linking $\mathbf{D}$ to $\mathbf{E}$ and $\mathbf{B}$ to $\mathbf{H}$ through the introduction of

$$\mathbf{D} = \varepsilon_0 \mathbf{E} + \mathbf{P}, \tag{4a}$$

$$\mathbf{B} = \mu_0 \mathbf{H} + \mathbf{M}. \tag{4b}$$

where ε_0, and μ_0 are the vacuum permittivity and permeability, $\mathbf{P} : \mathbb{R}^3 \times \mathbb{R} \mapsto \mathbb{R}^3$ the polarization and $\mathbf{M} : \mathbb{R}^3 \times \mathbb{R} \mapsto \mathbb{R}^3$ the magnetization. At this point, it may be mentioned that (4a) is of high interest for this work. Throughout the following derivations non-magnetic dispersive materials will be assumed because all concepts are applied to non-magnetic metallic structures. The magnetic polarization will

thus be considered to be zero. Further, the polarization $\mathbf{P}$ can be split into different contributing parts. Since metals consist of a rigid ion grid that is built of positive ion cores together with the locally fixed bound electrons (d-band) and the freely moving valence electrons (s-band), essentially the polarization of metals can be described by two mechanisms: on one hand the polarization of the free valence electrons $\mathbf{P}_f$ and on the other hand dipole polarizations due to the local displacement of bound electrons which is also known as background polarization $\mathbf{P}_\infty$ [11].

2.2 Nanoplasmonics

The plasmonic effect of nanoparticles is of increasing importance for various applications. For example in tumor therapy, nanoparticles are used to *burn* tumor cells without the necessity of a surgery. As nanoparticles can cause extreme local field enhancements in the range of 10^4 orders of magnitude, they allow to heat up tumor cells efficiently while the exciting fields and the radiation exposure for the surrounding tissues remain at low levels compared to classical radio therapy [12]. Also, nanoplasmonic effects are more and more used in terms of extreme light confinement, perfect lenses and photonic waveguides [13]-[14]-[15]. However, the consideration of plasmonic effects becomes necessary as soon as the electromagnetic skin depth is larger than the particles' dimensions itself. Thus, the fields can completely penetrate the particle and excite resonant oscillations [16]. Nevertheless, if the particle dimensions reach regions where electrons can show their full quantum nature [17], the hydrodynamic model which is used in this work is not applicable anymore and QM wave functions have to be completely taken into account. Since every metal, e.g. gold, copper, or an alkaline metal has different characteristics or material properties, dimensional arguments where nanoplasmonic effects should be considered or not are intrinsically limited. As a rule of thumb and often mentioned in literature [17], plasmonic effects for nanostructures should be taken into account when dimensions in the range of $\approx$ 1 nm - 25 nm occur while the incident wavelength is usually comparatively large and considered as plane wave [18].

2.3 The Drude model

The Drude model is a first step on the way to describe the dispersive behavior of metals. It assumes the electrons inside the metal to behave identically and be uncoupled, also known as the free electron gas. Further, this model assumes each electron to behave as a simple mass oscillator driven by an electrical field. The induced polarization due to the frequency-dependent electron movement leads to a frequency-dependent polarization (dispersion) [19]. Writing the equation of motion for a single electron in the form of

$$-e\mathbf{E}(t) = m_e\partial_{tt}\mathbf{x}(t) + m_e\gamma_c\partial_t\mathbf{x}(t), \tag{5}$$

and with $\mathbf{P}_f(t) = -ne\mathbf{x}(t)$, we have

$$\frac{e^2 n}{m_e \varepsilon_0}\varepsilon_0 \mathbf{E}(t) = \partial_{tt}\mathbf{P}_f(t) + \gamma_c \partial_t \mathbf{P}_f(t). \tag{6}$$

Here, e and m_e are the elementary charge and mass of an electron, respectively; $\mathbf{x} : \mathbb{R} \mapsto \mathbb{R}^3$ denotes the spatial displacement of one electron with respect to the time t. γ_c is the characteristic collision frequency defined by the inverse of the relaxation time of the free electron gas τ, and n the electron density of the gas. Typical values for γ_c at room temperature are in the order of $\gamma_c = 100$ THz for non-noble metals [19]. As the electrons are described in a free electron gas, the macroscopic polarization appears due to the displacement of charges. For simplicity purposes, the polarization due to free electrons $\mathbf{P}_f$ is represented by $\mathbf{P}$ in the following. With a harmonic time dependence $\mathbf{E}(t) = \mathbb{R}\{\underline{\mathbf{E}} \exp(-i\omega t)\}$, where i is the imaginary unit and underlined quantities are phasors, the Drude model yields

$$\underline{\mathbf{P}} = -\frac{ne^2}{m_e(\omega^2 + i\gamma_c\omega)}\underline{\mathbf{E}}. \tag{7}$$

Taking the polarization obtained in (7) together with (4a), the electric displacement can be written as

$$\begin{aligned} \underline{\mathbf{D}} &= \varepsilon_0 \underbrace{(1+\chi_b)}_{\varepsilon_\infty}\underline{\mathbf{E}} + \underline{\mathbf{P}}, \\ &= \left[\varepsilon_0\varepsilon_\infty - \frac{ne^2}{m_e(\omega^2 + i\gamma_c\omega)}\right]\underline{\mathbf{E}}, \\ &= \varepsilon_0 \varepsilon(\omega)\underline{\mathbf{E}}, \end{aligned} \tag{8}$$

with

$$\varepsilon(\omega) := \varepsilon_\infty - \frac{\omega_p^2}{\omega^2 + i\gamma_c\omega}, \tag{9}$$

where $\omega_p = \sqrt{\frac{ne^2}{\varepsilon_0 m_e}}$ is the plasma frequency of the free electron gas and χ_b the polarization due to bound electrons [19]. Since (9) is a complex number, it is appropriate to split the complex permittivity into real and imaginary part in order to discuss the behavior of metals in different frequency ranges with respect to the plasma

frequency. Separating (9) into $\varepsilon(\omega) = \varepsilon_1(\omega) + i\varepsilon_2(\omega)$ leads to

$$\varepsilon(\omega) = \varepsilon_\infty - \frac{\omega_p^2}{\omega^2 + \gamma_c^2} + i\frac{\gamma_c \omega_p^2}{\omega(\omega^2 + \gamma_c^2)}, \tag{10a}$$

$$\varepsilon_1(\omega) = \varepsilon_\infty - \frac{\omega_p^2}{\omega^2 + \gamma_c^2}, \tag{10b}$$

$$\varepsilon_2(\omega) = \frac{\gamma_c \omega_p}{\omega(\omega^2 + \gamma_c^2)}. \tag{10c}$$

2.4 The Drude-Lorentz model

The previously discussed Drude model provides a first approach for describing the dispersion of metals. Unfortunately, this description is not very accurate for noble metals in a frequency regime close to the plasma frequency ω_p. In this regime, the influence of interband effects because of bound electrons (d-band) increases and has to be taken into account. Without using a full QM model, the Drude-Lorentz model is a semi-classical extension of the classical Drude model. The Drude-Lorentz model extends the Drude model with an additional spring term $m_e\omega_b^2\mathbf{x}$ that represents the binding force of each electron to the positive ion cores. Since ω_b is a *global* parameter for each material, all electrons are assumed to behave equally and independently. Adding the Lorentz term for bound electrons to (5), the equation of motion reads

$$-e\mathbf{E}(t) = m_e\partial_{tt}\mathbf{x}(t) + m_e\gamma_c\partial_t\mathbf{x}(t) + m_e\omega_b^2\mathbf{x}(t). \tag{11}$$

Applying the harmonic time dependence as we did for (5) yields

$$\underline{\mathbf{x}} = \frac{e}{m_e(\omega^2 + i\omega\gamma_c - \omega_b^2)}\underline{\mathbf{E}}, \tag{12}$$

where γ_c is a damping factor for the electron oscillation around the ion. In a purely mathematical sense, the Drude-Lorentz model adds an additional pole by means of improving the fitting curve in comparison to the experimental data [9]. However, it is still based on physical considerations by taking QM effects into account in terms of the damping constant γ_c and the oscillation frequency ω_b. Thus, the Drude-Lorentz model provides a *second* order approach of the local response for metals where the free electrons are considered as a free electron gas including some binding forces to the ions.

The overall permittivity in the frequency domain of the local Drude and Drude-Lorentz model according to (10), (12) and by including the residual polarization

$\underline{\mathbf{P}}_\infty = \varepsilon_0\varepsilon_\infty\underline{\mathbf{E}}$, is expressed analogously by

$$\varepsilon_{tot} = \varepsilon_\infty - \frac{\omega_p^2}{\omega^2 + i\gamma_c\omega} - \Delta\varepsilon\frac{\omega_b^2}{\omega^2 + i\omega\gamma_c - \omega_b^2}, \tag{13a}$$

and separated into real and imaginary part

$$\begin{aligned}\varepsilon_1(\omega) &= \varepsilon_\infty - \frac{\omega_p^2}{\omega^2 + \gamma_c^2} - \Delta\varepsilon\frac{\omega_b^2(\omega^2 - \omega_b^2)}{\gamma_c^2\omega^2 + (\omega^2 - \omega_b^2)^2},\\ \varepsilon_2(\omega) &= \frac{\gamma_c\omega_p^2}{\omega(\omega^2 + \gamma_c^2)} + \Delta\varepsilon\frac{\omega_b^2\gamma_c\omega}{\gamma_c^2\omega^2 + (\omega^2 - \omega_b^2)^2},\end{aligned} \tag{13b}$$

where $\Delta\varepsilon$ is a weighting factor for the Drude-Lorentz impact. As a matter of completeness, it may be mentioned that a higher order fitting approach, such as Padé approximation [9], in order to better fit measured values e.g. by Johnson and Christy [20], is also possible. It may be pointed out that the presented models so far as well as higher order models remain in the scope of local responses and will not physically include any electron interactions. Although, non-local effects are naturally included in any experimental data.

2.5 Hydrodynamic modeling of the electron response

The assumption of an ideal free electron gas faces its limits when it comes to even smaller geometries with dimensions beyond tenth of nanometers [21],[17]. A cube with an edge length of 10 nm, for instance, would hit the critical regime. But also two thick nanowires being placed narrowly with a gap size in the range of $\approx$ 1 nm - 5 nm would show a different behavior if electron interactions were considered. Among others, QM codes are available which take the full wave character of electrons into account. Although these solvers provide a very accurate model of the underlying physics, the computational effort is so heavy that it makes realistic geometries unaffordable. Another approach in order to include quantum tunneling for narrow gap structures is the Quantum-Corrected Model (QCM) that adds a tunneling term to the local Drude model. This term scales with the gap size and converges to the purely classical Drude model for larger distances ($>$ 5 nm) [22] until it vanishes completely.

Within this work the focus is put on a non-local model in terms of an electron fluid moving against a positive ion background similar to the one fluid description for plasmas [23]. This approach includes inter-electron coupling modeled by a hydrodynamic pressure (Coulomb interactions in a Fermi gas) [24]. As an interesting fact it turns out that starting from the hydrodynamic model and finally neglecting the non-local impact, the resulting polarization is equivalently described as the local Drude model (6). In addition to the hydrodynamic model, different approaches with

the purpose of describing the non-local response can be found in literature [25]. Our work does only consider a linearized model as shown below. Nevertheless, various publications exist on SHG (Second Harmonic Generation - also called frequency doubling). This is a non-linear optical process, in which photons with the same frequency interacting with a non-linear material are effectively *combined* to generate new photons with twice the energy, and therefore twice the frequency and half the wavelength of the initial photons. SHG, as an even order non-linear optical effect, is only allowed in media without inversion symmetry. It is a special case of sum frequency generation.

2.5.1 The linearized fluid model

In the following part, the Linearized Fluid (LF) equation for electron gas is derived from the general non-linear case. The general fluid equation together with the quantum pressure term on the right hand side in (14a) allows different models for the electron interactions. Thus, the choice of this term has to be taken carefully in order to correctly include the underlying physics. Detailed descriptions of this term can be found in [26] while a relatively simple approach is going to be considered in the scope of this work. With the electron mass m_e and a damping constant γ the hydrodynamic electron description reads

$$m_e(\partial_t + \mathbf{v}\cdot\nabla)\mathbf{v} = -e[\mathbf{E} + \mathbf{v}\times\mathbf{B}] - m_e\gamma\mathbf{v} - \nabla\left(\frac{\delta g[n]}{\delta n}\right), \tag{14a}$$

together with the continuity equation

$$0 = \partial_t n + \nabla\cdot(n\mathbf{v}), \tag{14b}$$

where $\mathbf{v} : \mathbb{R}^3 \times \mathbb{R} \mapsto \mathbb{R}^3$ represents the fluid velocity and the last right term of (14a) is the QM influence briefly mentioned above. Linearizing the velocity, magnetic, and density fields around $\{\mathbf{v}_0, \mathbf{B}_0, n_0\}$ leads to

$$\begin{aligned} \mathbf{v}(\mathbf{r},t) &\approx \mathbf{v}_0 + \mathbf{v}_1(\mathbf{r},t), \\ \mathbf{B}(\mathbf{r},t) &\approx \mathbf{B}_0 + \mathbf{B}_1(\mathbf{r},t), \\ n(\mathbf{r},t) &\approx n_0 + n_1(\mathbf{r},t), \end{aligned} \tag{15a}$$

where we consider $\mathbf{v}_0 = \mathbf{B}_0 = \partial_t n_0 \equiv 0$ since the fluid is considered to be non moving, without any static magnetic fields, and with a constant density that can locally change due to $n_1(\mathbf{r}, t)$. Further, the second term on the left hand side and the magnetic term on the right side of (14a) vanish due to (15a) and by neglecting higher order terms. Inspired by [27], the pressure term and the equation of continuity simplify to

$$\nabla \left(\frac{\delta g[n]}{\delta n} \right) \approx m_e \beta^2 \frac{1}{n_0} \nabla n_1, \tag{15b}$$

$$\partial_t n_1 = -n_0 \nabla \cdot \mathbf{v}_1, \tag{15c}$$

and thus for (14a)

$$m_e \partial_t \mathbf{v} = -e\mathbf{E} - m_e \gamma \mathbf{v} - m_e \beta^2 \frac{1}{n_0} \nabla n_1. \tag{15d}$$

The choice of the quantum related parameter β is a crucial point in this model. For the moment, this parameter is left arbitrarily even though it is fairly often set to $\sqrt{3/5} v_F$ with the Fermi velocity v_F [26]. Where the LF equation still distinguishes between n_0 and n_1 the subscript for the velocity vector has already been ignored by means of $\mathbf{v}_1 \to \mathbf{v}$. Differentiating (15d) with respect to the time t and inserting (15b), (15c) yields

$$m_e \partial_{tt} \mathbf{v} = -e \partial_t \mathbf{E} - m_e \gamma \partial_t \mathbf{v} + m_e \beta^2 \nabla (\nabla \cdot \mathbf{v}), \tag{16}$$

where permutability of the time and the spatial derivatives is assumed. Multiplying by $-ne$, where n will denote n_1, gives

$$0 = \partial_{tt} \mathbf{J} + \gamma \partial_t \mathbf{J} - \beta^2 \nabla (\nabla \cdot \mathbf{J}) - \omega_p^2 \varepsilon_0 \partial_t \mathbf{E}, \tag{17}$$

where $\mathbf{J} = -ne\mathbf{v}$ is the current density of the unbound electrons in the fluid. According to subsection 2.3, the polarization $\mathbf{P} = -ne\mathbf{x}$ is defined as the displacement of the charge density and thus

$$\partial_t \mathbf{P} = -ne \partial_t \mathbf{x} = -ne\mathbf{v} = \mathbf{J}. \tag{18}$$

Together with (17), the polarization relation reads

$$0 = \partial_{ttt} \mathbf{P} + \gamma \partial_{tt} \mathbf{P} - \beta^2 \partial_t \nabla (\nabla \cdot \mathbf{P}) - \omega_p^2 \varepsilon_0 \partial_t \mathbf{E}. \tag{19}$$

Integration with respect to the time finally yields

$$0 = \partial_{tt} \mathbf{P} + \gamma \partial_t \mathbf{P} - \beta^2 \nabla (\nabla \cdot \mathbf{P}) - \omega_p^2 \varepsilon_0 \mathbf{E}. \tag{20}$$

This integration assumes (20) to be fulfilled for any initial time $t = T_0$. It is quite interesting to compare the last equation with the results previously obtained with the local Drude model. Although the physical considerations are seriously different, the local response (6) is only extended by an additional term $-\beta^2\nabla(\nabla\cdot\mathbf{P})$ for the linearized non-local fluid model. Nevertheless, together with Maxwell's equations, this term complicates the system of PDEs significantly. While the polarization was simply described by an ODE (6), the non-local model requires the additional solution of a PDE (20). For the rest of the work, we will stick to the formulation given in (17).

2.5.2 Analysis of the linearized non-local model

After having found a description of the polarization of bound and free electrons, the entire considered physics is modeled by Maxwell's equations for the electrodynamic contribution, the remaining background polarization $\mathbf{P}_\infty = \mathbf{P}_b$ for the bound electrons and the LF model for the free electron gas. This total system of PDE reads

$$\begin{aligned} \nabla\times\mathbf{H} &= \partial_t\mathbf{D}, \\ \nabla\times\mathbf{E} &= -\mu_0\partial_t\mathbf{H}, \qquad (21a)\\ \partial_t\mathbf{D} &= \varepsilon_0\varepsilon_\infty\partial_t\mathbf{E}+\mathbf{J}, \\ \omega_p^2\varepsilon_0\partial_t\mathbf{E} &= \partial_{tt}\mathbf{J}+\gamma\partial_t\mathbf{J}-\beta^2\nabla(\nabla\cdot\mathbf{J}), \qquad (21b)\end{aligned}$$

where all currents are considered as a charge displacement in terms of polarization. In general, PDE can be cathegorized into three categories: elliptic, parabolic or hyperbolic. In order to show the hyperbolicity of Maxwell's equations, Ampere's and Faraday's law can be written in a conservative form. Leaving out unbound polarizations and currents for a moment, i.e. $\mathbf{J}\equiv 0$ in (21), (3) reads

$$0 = \partial_t\mathbb{L}\mathbf{u}+\nabla\cdot\mathbf{F}(\mathbf{u}), \qquad (22)$$

with

$$\mathbf{u} = \begin{pmatrix}\mathbf{E}\\ \mathbf{H}\end{pmatrix}, \qquad (23)$$

$$\nabla\cdot\mathbf{F} = \sum_{\alpha=1}^{3}\mathbb{N}^\alpha\partial_\alpha\mathbf{u}, \qquad (24)$$

where $\mathbb{L}$ contains the material properties $\{\varepsilon_0\varepsilon_\infty,\mu_0\}$, $\mathbb{N}^\alpha$ represents the curl operator of system (21) and α the spatial coordinate. As all materials are considered to be constant in time, system (22) can be rewritten as

$$0 = \partial_t\mathbf{u}+\mathbb{L}^{-1}\nabla\cdot\mathbf{F}(\mathbf{u}). \qquad (25)$$

After having written Maxwell's equations in a conservative form, the following definition provides a criterion to investigate the hyperbolicity of (22).

Definition 1 *[28] A first order operator*

$$\boldsymbol{\mathcal{L}} = \partial_t + \sum_\alpha \boldsymbol{\mathcal{A}}^\alpha \partial_\alpha + \boldsymbol{\mathcal{B}}, \tag{26}$$

is said to be hyperbolic if the corresponding symbol $\boldsymbol{\xi} \mapsto \boldsymbol{\mathcal{A}}(\boldsymbol{\xi})$*, with* $\boldsymbol{\mathcal{A}}(\xi) := \sum_\alpha \boldsymbol{\xi}_\alpha \boldsymbol{\mathcal{A}}^\alpha$*, satisfies*

$$\sup_{\xi \in \mathcal{R}^d} \| \exp(i\boldsymbol{\mathcal{A}}(\boldsymbol{\xi})) \| < +\infty. \tag{27}$$

The system $\boldsymbol{\mathcal{L}} u = 0$ *with* $\boldsymbol{\mathcal{L}}$ *and operator (whatever* $\boldsymbol{\mathcal{B}}$ *is) that satisfies the latter mentioned condition is called a hyperbolic system of first order PDEs.*

Definition 1 provides a criterion for the hyperbolicity of system (22). Defining, $\forall \xi \in \mathbb{R}^3$ with $\xi = (\xi_1, \xi_2, \xi_3)^T$, $\| \xi \| = 1$

$$\mathbb{A}(\xi) = \mathbb{L}^{-1} \left(\xi_1 \mathbb{N}^1 + \xi_2 \mathbb{N}^2 + \xi_3 \mathbb{N}^3 \right), \tag{28}$$

and claiming all eigenvalues λ_n of $\mathbb{A}$ to be real is indeed equivalent and easier to show than Definition 27. Thus, we diagonalize matrix $\mathbb{A}$ by means of

$$\mathbb{A} = \mathbb{S}^{-1} \mathbb{D} \mathbb{S}, \tag{29}$$

with

$$\mathbb{S} = \left(\nu_1, \dots, \nu_6 \right), \tag{30}$$

$$\mathbb{D} = \text{diag}\{\lambda_1, \dots, \lambda_6\}, \tag{31}$$

where $\nu_n \in \mathbb{C}^{6\times 1}$ and $\lambda_n \in \mathbb{C}$ are the eigenvectors and corresponding eigenvalues of $\mathbb{A}$, respectively. Here, $\mathbb{C}$ denotes the set of complex numbers. Evaluating (29) gives

$$\mathbb{A} = \begin{pmatrix} 0 & 0 & 0 & 0 & -\frac{\xi_3}{\varepsilon_0 \varepsilon_\infty} & \frac{\xi_2}{\varepsilon_0 \varepsilon_\infty} \\ 0 & 0 & 0 & \frac{\xi_3}{\varepsilon_0 \varepsilon_\infty} & 0 & -\frac{\xi_1}{\varepsilon_0 \varepsilon_\infty} \\ 0 & 0 & 0 & -\frac{\xi_2}{\varepsilon_0 \varepsilon_\infty} & \frac{\xi_1}{\varepsilon_0 \varepsilon_\infty} & 0 \\ 0 & \frac{\xi_3}{\mu} & -\frac{\xi_2}{\mu} & 0 & 0 & 0 \\ -\frac{\xi_3}{\mu} & 0 & \frac{\xi_1}{\mu} & 0 & 0 & 0 \\ \frac{\xi_2}{\mu} & -\frac{\xi_1}{\mu} & 0 & 0 & 0 & 0 \end{pmatrix},$$

and thus for the eigenvalues

$$\boldsymbol{\lambda}(\xi) = \begin{Bmatrix} 0 & 0 & -c\,\|\xi\| & -c\,\|\xi\| & c\,\|\xi\| & c\,\|\xi\| \end{Bmatrix}, \tag{32}$$

with the speed of light $c = 1/\sqrt{\mu_0\varepsilon_0\varepsilon_\infty}$. The first two eigenvalues are the electrostatic modes and the remaining four correspond to forth and backwards traveling waves. Extending Maxwell's equations to system (21b) does not necessarily preserve the hyperbolicity as shown above and claims further investigations. Including the unbound polarization $\mathbf{P}_f$ leads to a second order PDE because of the double differential operator $\nabla(\nabla\cdot)$ which is applied to the polarization due to the fluid description. This can be overcome by introducing an auxiliary quantity Q in order to transform (21b) to a first order PDE system. The resulting system of PDEs is equivalent to (21) rewritten as

$$\begin{aligned} \mu_0\partial_t\mathbf{H} + \nabla\times\mathbf{E} &= 0, \\ \varepsilon_0\varepsilon_\infty\partial_t\mathbf{E} - \nabla\times\mathbf{H} &= -\mathbf{J}, \\ \partial_t\mathbf{J} - \beta^2\nabla Q &= \omega_p^2\varepsilon_0\mathbf{E} - \gamma\mathbf{J}, \\ \partial_t Q - \nabla\cdot\mathbf{J} &= 0, \end{aligned} \tag{33}$$

and for the conservative form (22) yields

$$\mathbf{u} = \begin{pmatrix} \mathbf{E} & \mathbf{H} & \mathbf{J} & Q \end{pmatrix}^T, \tag{34}$$

for the vector of unknowns, where $(\,\cdot\,)^T$ denotes the transposed matrix. Q is a scalar field and indeed represents the charge density. In fact, the fourth equation in (33) is the continuity equation and reduces the order of (33) to a system of linear PDE. Analogously to (22) for the hydrodynamical model, the matrix $\mathbb{A}$ that corresponds becomes

$$\tilde{\mathbb{A}}(\xi) = \begin{pmatrix} \mathbb{A}_{\mathbf{E}}(\xi) & & \mathbb{O}_{6\times4} \\ & & \beta^2\xi_1 \\ \mathbb{O}_{3\times6} & \mathbb{O}_{3\times3} & \beta^2\xi_2 \\ & & \beta^2\xi_3 \\ \mathbb{O}_{1\times6} & \xi_1\ \xi_2\ \xi_3 & 0 \end{pmatrix}, \tag{35}$$

where $\tilde{\mathbb{A}}(\xi) \in \mathbb{R}^{10\times10}$. $\mathbb{O}$ contains only zeroes. Solving the eigenvalue problem for (35) gives the previously seen electromagnetic and four additional waves

$$\boldsymbol{\lambda}(\|\xi\|) = \begin{Bmatrix} 0 & 0 & 0 & 0 & -c\,\|\xi\| & -c\,\|\xi\| & c\,\|\xi\| & c\,\|\xi\| & -\beta & \beta \end{Bmatrix}. \tag{36}$$

Since the underlying physics of the non-local contribution is hidden in the quantum related parameter β, it is kind of straightforward that the eigenvalues depend on β. More important for the analysis of the hyperbolicity, however, is the fact that

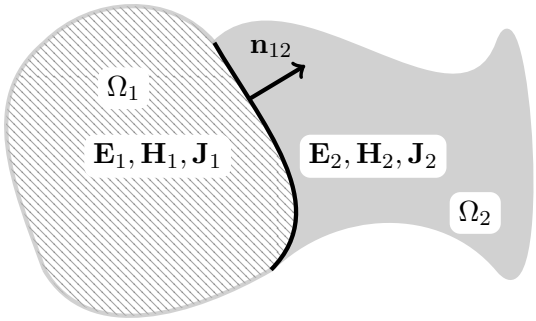

Figure 1: Boundary interface between two arbitrary media Ω_1 and Ω_2. The surface normal and field quantities in each domain are denoted by $\mathbf{n}_{12}$ and $\mathbf{E}_{1,2}, \mathbf{H}_{1,2}, \mathbf{J}_{1,2}$, respectively.

all eigenvalues $\lambda_n \in \mathbb{R}$ remain elements of the real number set. Thus, according to Definition 1 the system (33) is also hyperbolic. Analogous to the electrodynamic case, the two new eigenvalues that depend on beta can be interpreted as the speed of hydrodynamic waves. Those waves are the propagating bulk plasmons that occur due to non-locality.

2.5.3 Boundary value problem

So far, we have not dealt with any spatial domain limitations, i.e. boundaries. We will now set up a boundary value problem where the junction from a dispersive to a non-dispersive regime will be a central point. For the numerical treatment, boundary conditions need to be specified. The boundary conditions at an interface between two different media for the $\mathbf{E}$ and $\mathbf{H}$ fields are given by

$$\mathbf{n}_{12} \times (\mathbf{E}_2 - \mathbf{E}_1) = 0, \tag{37}$$

$$\mathbf{n}_{12} \times (\mathbf{H}_2 - \mathbf{H}_1) = \mathbf{J}_s, \tag{38}$$

where $\mathbf{n}_{12}$ is the surface normal pointing from medium 1 to 2 and $\mathbf{J}_s$ the surface current. Figure 1 illustrates the interface between two different media. Since our metals are *not* perfectly conducting materials, the surface current and density $\mathbf{J}_s \equiv 0$ has to be zero [10]. These interface conditions would be adequate for a local dispersion model where no bulk plasmons can appear. For the non-local dispersion, this is not the case anymore and bulk plasmons can be excited [21]. This however leads to the requirement of an artificial boundary condition. As in our work the free electrons of a metal are described by a hydrodynamic model and quantum effects like tunneling are left out, it is physically reasonable to prohibit that elec-

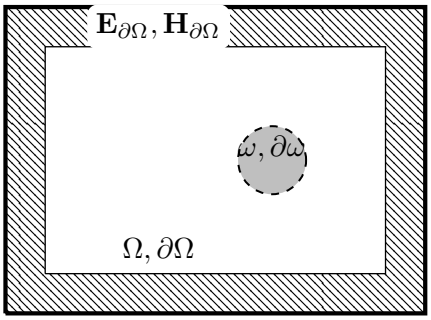

Figure 2: BVP for the non-local dispersion model according to Figure 3. Ω represents the domain around the dispersive nanostructure e.g. vacuum while ω is the dispersive domain where polarization currents are allowed. The boundary $\partial\Omega$ illustrated the junction to the infinite space. In terms of numerics, this boundary is of high importance, because the infinite space must be truncated and approximated with an open boundary.

trons escape while they can freely move inside a metal. Motivated by this, Moreau *et al.* propose in [1] the boundary condition

$$\mathbf{n}_{12} \cdot (\mathbf{J}_2 - \mathbf{J}_1) = 0, \tag{39}$$

with

$$\mathbf{J}_2 \equiv 0, \tag{40}$$

for the current density, where $\mathbf{J}_2$ are the currents outside the dispersive regime. Taking a look at Figure 2, the entire boundary value problem for the non-dispersive regime Ω reads

$$\mathbb{L}\partial_t \mathbf{u} + \nabla \cdot \mathbf{F}(\mathbf{u}) = 0 \quad \text{on } \Omega \times \mathbb{R}^+, \tag{41a}$$
$$\mathbf{D}(\mathbf{u}) = 0 \quad \text{on } \partial\Omega \times \mathbb{R}^+, \tag{41b}$$

where $\mathbf{D}$ handles the boundary conditions on $\partial\Omega$. Let us consider a dispersive media in ω. One has analoguously

$$\mathbb{L}_d \partial_t \mathbf{u}_d + \nabla \cdot \mathbf{F}_d(\mathbf{u}_d) = \mathbb{B}_d \mathbf{u}_d \quad \text{on } \omega \times \mathbb{R}^+, \tag{42a}$$
$$\mathbf{n}_{\omega,\Omega} \cdot \mathbf{J}_\omega = 0 \quad \text{on } \partial\omega \times \mathbb{R}^+, \tag{42b}$$
$$\mathbf{n}_{\omega,\Omega} \times (\mathbf{E}_\Omega - \mathbf{E}_\omega) = 0 \quad \text{on } \partial\omega \times \mathbb{R}^+, \tag{42c}$$
$$\mathbf{n}_{\omega,\Omega} \times (\mathbf{H}_\Omega - \mathbf{H}_\omega) = 0 \quad \text{on } \partial\omega \times \mathbb{R}^+, \tag{42d}$$

where the index d distinguishes the conservation law for the non-dispersive and dispersive regime according to section 2.5.2.

2.6 Energy preservation

Energy preservation can be understood as a figure of merit of a physical model as the total energy stored in a physically motivated system must never increase. Additionally, this property should be consequently kept when it comes to numerical algorithms. Defining the energy as

$$\mathcal{E}(t) := \frac{1}{2}\left\{\mu_0\omega_p^2\varepsilon_0\|\mathbf{H}\|^2_{\mathcal{L}^2(\Omega)} + \varepsilon_\infty\varepsilon_0^2\omega_p^2\|\mathbf{E}\|^2_{\mathcal{L}^2(\Omega)} + \|\mathbf{J}\|^2_{\mathcal{L}^2(\Omega)} + \beta^2\|Q\|^2_{\mathcal{L}^2(\Omega)}\right\}, \tag{43}$$

assuming that each field quantity shows a sufficient regularity in space and $\mathcal{C}^1$ in time, (43) together with (33) leads to

$$\begin{aligned}
\partial_t\mathcal{E}(t) =& -\omega_p^2\varepsilon_0\int_\Omega(\nabla\times\mathbf{E})\cdot\mathbf{H}\,\mathrm{d}^3\mathbf{r}\\
&+\varepsilon_0\omega_p^2\left(\int_\Omega(\nabla\times\mathbf{H})\cdot\mathbf{E}\,\mathrm{d}^3\mathbf{r} - \int_\Omega\mathbf{J}\cdot\mathbf{E}\,\mathrm{d}^3\mathbf{r}\right)\\
&+\varepsilon_0\omega_p^2\int_\Omega\mathbf{E}\cdot\mathbf{J}\,\mathrm{d}^3\mathbf{r} - \gamma\int_\Omega\mathbf{J}\cdot\mathbf{J}\,\mathrm{d}^3\mathbf{r} + \beta^2\int_\Omega\nabla Q\cdot\mathbf{J}\,\mathrm{d}^3\mathbf{r}\\
&+\beta^2\int_\Omega Q\nabla\cdot\mathbf{J}\,\mathrm{d}^3\mathbf{r},\\
=& -\gamma\|\mathbf{J}\|_{\mathcal{L}^2(\Omega)} \leq 0,
\end{aligned} \tag{44}$$

where we have assumed that $\partial\Omega$ is a perfectly electric conducting boundary and that currents vanish outside Ω, meaning vanishing surface integrals in

$$\begin{aligned}
\int_\Omega(\nabla\times\mathbf{E})\cdot\mathbf{H}\,\mathrm{d}^3\mathbf{r} &= \int_\Omega(\nabla\times\mathbf{H})\cdot\mathbf{E}\,\mathrm{d}^3\mathbf{r} - \int_{\partial\Omega}(\mathbf{H}\times\mathbf{E})\cdot\mathbf{n}\,\mathrm{d}^2\mathbf{r},\\
&= \int_\Omega(\nabla\times\mathbf{H})\cdot\mathbf{E}\,\mathrm{d}^3\mathbf{r},
\end{aligned} \tag{45}$$

$$\int_\Omega(\nabla Q\cdot\mathbf{J} + Q\nabla\cdot\mathbf{J})\,\mathrm{d}^3\mathbf{r} = \int_{\partial\Omega}Q\mathbf{J}\cdot\mathbf{n}\,\mathrm{d}^2\mathbf{r} = 0, \tag{46}$$

where $\mathbf{n}$ denotes the surface normal pointing outwards $\partial\Omega$. The result obtained in (44) shows the strict preservation of the energy $\partial_t\mathcal{E}(t) = 0$ for a collision free model and does also drive dissipation if collisions (damping) are taken into account.

2.7 Mode splitting in the two-dimensional case

Considering a 2d computational domain in the x, y plane infinite in the z-direction, without any z dependency of the fields, all derivatives with respect to z vanish. Thus, as shown below, the total solution of (21b) can be separated into two independent sets of equations. Each set provides a solution where either the electric or magnetic field has only one spatial component and the corresponding magnetic or electric field is only polarized in the perpendicular plane, respectively. These solutions are also known as TM and TE modes of the electromagnetic field. Expressing the differential operators and field values component-by-component and crossing out the y derivatives, (21b) can be expressed as

$$\begin{aligned}
\omega_p^2\varepsilon_0\partial_t E_x &= \partial_{tt}J_x + \gamma\partial_t J_x - \beta^2(\partial_{xx}J_x + \partial_{xy}J_y + \cancel{\partial_{xz}}J_z),\\
\omega_p^2\varepsilon_0\partial_t E_y &= \partial_{tt}J_y + \gamma\partial_t J_y - \beta^2(\partial_{yx}J_x + \partial_{yy}J_y + \cancel{\partial_{yz}}J_z),\\
\omega_p^2\varepsilon_0\partial_t E_z &= \partial_{tt}J_z + \gamma\partial_t J_z - \beta^2(\cancel{\partial_{zx}}J_x + \cancel{\partial_{zy}}J_y + \cancel{\partial_{zz}}J_z),
\end{aligned} \tag{47}$$

while Faraday's and Ampère's laws become

$$\begin{pmatrix} \partial_y E_z - \cancel{\partial_z} E_y \\ \cancel{\partial_z} E_x - \partial_x E_z \\ \partial_x E_y - \partial_y E_x \end{pmatrix} = -\mu_0\partial_t\mathbf{H}, \tag{48}$$

$$\begin{pmatrix} \partial_y H_z - \cancel{\partial_z} H_y \\ \cancel{\partial_z} H_x - \partial_x H_z \\ \partial_x H_y - \partial_y H_x \end{pmatrix} = \varepsilon_0\varepsilon_\infty\partial_t\mathbf{E} + \mathbf{J}. \tag{49}$$

Seperation into differently polarized modes leads to

$$\begin{aligned}
\partial_y E_z &= -\mu_0\partial_t H_x,\\
-\partial_x E_z &= -\mu_0\partial_t H_y,\\
\partial_x H_y - \partial_y H_x &= \varepsilon_0\varepsilon_\infty\partial_t E_z + J_z,\\
\omega_p^2\varepsilon_0\partial_t E_z &= \partial_{tt}J_z + \gamma\partial_t J_z,
\end{aligned} \tag{50}$$

for the TM mode and similarly for the TE mode

$$\begin{aligned}
\partial_y H_z &= \varepsilon_0\varepsilon_\infty\partial_t E_x + J_x + J_x,\\
-\partial_x H_z &= \varepsilon_0\varepsilon_\infty\partial_t E_y + J_y + J_y,\\
\partial_x E_y - \partial_y E_x &= -\mu_0\partial_t H_z,\\
\omega_p^2\varepsilon_0\partial_t E_x &= \partial_{tt}J_x + \gamma\partial_t J_x - \beta^2(\partial_{xx}J_x + \partial_{xz}J_z),\\
\omega_p^2\varepsilon_0\partial_t E_y &= \partial_{tt}J_y + \gamma\partial_t J_y - \beta^2(\partial_{yx}J_y + \partial_{yy}J_y).
\end{aligned} \tag{51}$$

Obviously, system (50) has a z polarized electrical field $\mathbf{E} = E_z\mathbf{e}_z$ with the corresponding transverse magnetic field $\mathbf{H} = H_x\mathbf{e}_x + H_y\mathbf{e}_y$, where $\mathbf{e}_u, u \in \{x, y, z\}$ are

the cartesian basis vectors. Equally, the solution for (51) shows a magnetic polarization in z direction $\mathbf{H} = H_z\mathbf{e}_z$ with the corresponding transverse electric field $\mathbf{E} = E_x\mathbf{e}_x + E_y\mathbf{e}_y$. This is a remarkable result because only the TE mode is able to excite a non-local polarization in the 2d case while the TM mode remains totally local. For the purpose of studying non-local effects, it is sufficient to consider (51) regardless to (50).

2.8 Comparison of the local and non-local model

Local versus non-local modeling of the dispersion caused by electron interaction with the incident wave has been discussed in the previous sections. In the following, a direct comparison of both models is made. Most of the results have been presented in [21] by using a 2d infinitely long nanowire as a benchmark example. While local dispersion models show exactly one resonance peak for this geometry, the non-locality causes more resonances due to bulk plasmons. These confined longitudinal modes are excited because of the electron-electron coupling within the Fermi gas. That effect is brought by the $\nabla(\nabla\cdot)$ term in the fluid equation and weighted with the quantum related parameter β. In order to compare the underlying physics of both

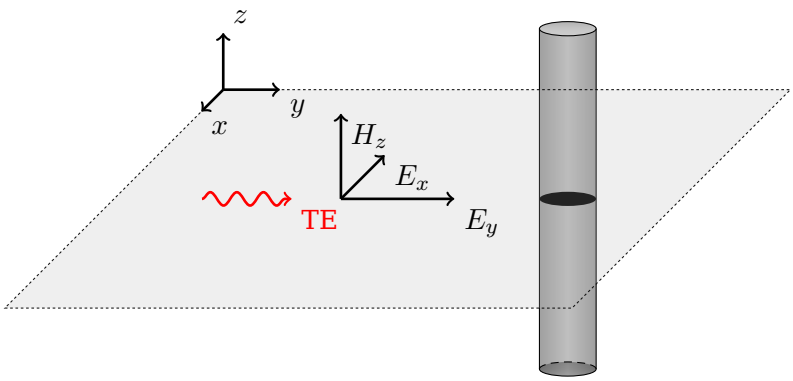

Figure 3: Infinitely long nanowire is illuminated by an electric field that is polarized perpendicular to the cylinder axis. Due to the translational invariance in the z direction, the 3d geometry is reduced to a 2d problem.

models, it is reasonable to select a simple model for which an analytical solution exists. For this purpose, the above mentioned geometry has been chosen. The analytical solution is obtained for a harmonic time dependency and thus system (21b) reads

$$\nabla\times\nabla\times\underline{\mathbf{E}} = \frac{\omega^2}{c^2}\underline{\mathbf{E}} + i\omega\mu_0\underline{\mathbf{J}}, \tag{52a}$$

$$i\omega\omega_p^2\varepsilon_0\underline{\mathbf{E}} = \beta^2\nabla(\nabla\cdot\underline{\mathbf{J}}) + \omega(\omega+i\gamma)\underline{\mathbf{J}}, \tag{52b}$$

where c is the speed of light in vacuum and ω a given pulsation. For the moment, the background polarization $\mathbf{P}_\infty$ is left out, but could be easily taken into account [19]. The $\nabla(\nabla\cdot)$ term can be split into a $\nabla\times\nabla$ term and a Laplacian term by the help of $\nabla(\nabla\cdot\mathbf{A}) = \nabla\times\nabla\times\mathbf{A} - \nabla^2\mathbf{A}$. However, some authors [29]-[30] consider a curl-free approximation for $\underline{\mathbf{E}}$ that leads to a curl-free $\underline{\mathbf{J}}$ in consequence. As a matter of fact, spurious resonances will appear because that assumption is only made in (52a) and not *enforced* for the solution of $\underline{\mathbf{E}}$ and $\underline{\mathbf{J}}$ as discussed in detail in [21] (splitting the fields in a div and curl free field and solving both cases separately). According to the previously defined boundary value problem, the curl-free approximation does also require an artificial boundary condition ($\mathbf{n}\times\underline{\mathbf{J}}$) as summarized in Table 1. The

Table 1: Summary of the three different response models. V is the volume of the nanostructure and ∂V its boundary. $\mathbf{L}_J$ is the differential operator in (52b). (Taken from [21]).

	$\mathbf{r}\in$ V		$\mathbf{r}\in\partial V$		$\mathbf{r}\notin$ V
	$\nabla\times\underline{\mathbf{J}}$	$\mathbf{L}_J$	$\mathbf{n}\cdot\underline{\mathbf{J}}$	$\mathbf{n}\times\underline{\mathbf{J}}$	$\underline{\mathbf{J}}$
Local	$\neq 0$	0	0	$\neq 0$	0
Non-local	$\neq 0$	$\beta^2\nabla(\nabla\cdot)$	0	$\neq 0$	0
Non-local, curl-free	0	$\beta^2\nabla^2$	0	0	0

analytical solution for a dispersive infinitely long wire can be calculated with an extended Mie theory developed in [31] where the calculated figure of merit is the extinction cross-section σ_{ext}. According to [21], the cross-section is given by

$$\sigma_{ext} = -\frac{2}{k_0 a}\sum_{n=-\infty}^{\infty}\Re\{\underline{a}_n\}, \tag{53}$$

where a is the radius of the wire, $k_0 = \omega/c$ the vacuum wave vector and a_n the Bessel-function expansion coefficient for the scattered fields. Taking a look at Figure 4, the question arises if and which additional resonances of the non-local models are physical or not. Indeed, the resonances labeled with P2 for the non-local model without the curl-free assumption (green line) are physical. These resonances exist due to bulk plasmons that do not exist in the local model and thus cannot be seen in the blue dashed curve. Contrarily, the curl-free assumption leads to spurious resonances for frequencies which are lower and beyond the plasma frequency ω_p. Although resonances above the plasma frequency are quite physical in the non-local case, they appear at different frequencies for the curl-free model with respect to the full hydrodynamic description. In addition, a blue shift for the non-local models appears with respect to the local one. Even though this blue shift appears in theory as well as in experiments, the physical explanation is not obvious. Two main effects, quantum confinement of single-particle states and confinement of collectives modes, might cause the frequency shift and are extensively discussed for nanospheres in

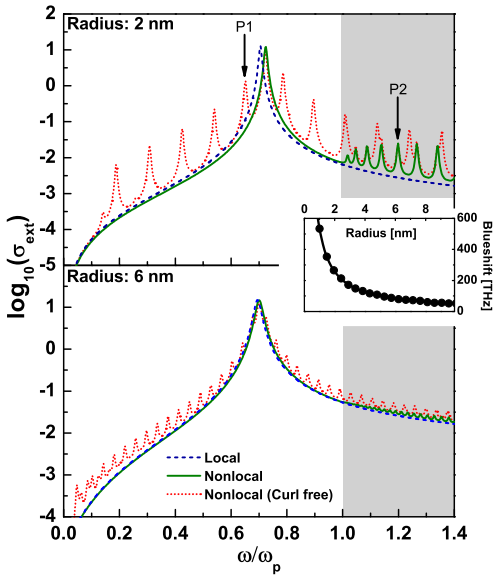

Figure 4: *From [21].* Extinction cross-sections σ_{ext} as a function of frequency for TE-polarized light normally incident on a metallic cylinder in vacuum. Parameters for Au as in [32] $\hbar\omega_p = 8.812$ eV, $\hbar\gamma = 0.0752$ eV, and $v_F = 1.39$ m/s. Inset: frequency shift of the maximum $\sigma_{ext}(\omega)$ for non-local against local response, as a function of radius.

[33]. Both enter the calculations through the pressure term in the non-local fluid description and cannot easily be distinguished within the semi-classical theory. Although the underlying physics may interact in detail, it is sufficient for this work to be aware of the occurring blueshift and bulk plasmon resonances due to non-locality.

2.9 Renormalization

We now want to normalize system (33) in order to simplify the equations and to focus on the quantities that change within space. Defining the vacuum impedance and speed of light

$$Z_0 = \sqrt{\frac{\mu_0}{\varepsilon_0}}, \tag{54}$$

$$c_0 = \frac{1}{\sqrt{\mu_0 \varepsilon_0}}, \tag{55}$$

and substituting the original quantities by

$$\left\{\tilde{\mathbf{H}}, \tilde{\mathbf{E}}, \tilde{\mathbf{J}}, \tilde{Q}, \tilde{t}, \tilde{\beta}^2, \tilde{\gamma}, \tilde{\omega_p}\right\} := \left\{Z_0\mathbf{H}, \mathbf{E}, Z_0\mathbf{J}, c_0 Z_0 Q, c_0 t, \frac{\beta^2}{c_0^2}, \frac{\gamma}{c_0}, \frac{\omega_p}{c_0}\right\}, \tag{56}$$

yields for system (33)

$$\begin{aligned} \partial_{\tilde{t}}\tilde{\mathbf{H}} + \nabla \times \tilde{\mathbf{E}} &= 0, \\ \varepsilon_\infty \partial_{\tilde{t}}\tilde{\mathbf{E}} - \nabla \times \tilde{\mathbf{H}} &= -\tilde{\mathbf{J}}, \\ \partial_{\tilde{t}}\tilde{\mathbf{J}} - \tilde{\beta}^2 \nabla \tilde{Q} &= \tilde{\omega_p}^2 \tilde{\mathbf{E}} - \tilde{\gamma}\tilde{\mathbf{J}}, \\ \partial_{\tilde{t}}\tilde{Q} - \nabla \cdot \tilde{\mathbf{J}} &= 0. \end{aligned} \tag{57}$$

This renormalized version of system (33) is not used in the following development of the DGTD scheme, but is has been adopted for the actual implementation.

3 DGTD scheme

The previous section presented and discussed the physical framework we consider in this work. Since many applications in nanophotonics have complicated structures, numerical treatment is unavoidable. With a numerical solver, it is essentially possible to simulate arbitrary structures. As we are dealing with hyperbolic equations, we have a system of PDEs that contain partial derivatives in space and time. In this section we first describe a spatial discretization approach of this system based on a discontinuous Galerkin (DG) formulation. In the DG framework, numerical fluxes[2] have to be introduced as the method naturally leads to discontinuities. This work only considers centered fluxes but further extensions to other fluxes could be considered. The obtained semi-discrete system is then time integrated using an explicit scheme. A stability analysis is outlined for the semi-discrete scheme and the fully-discrete one, afterwards.

3.1 The discontinuous Galerkin method

The DG method was firstly proposed in the context of neutron transport problems by Reed and Hill in [34]. In the following years, the method has become very popular and has been applied to a vast field of computational physics and engineering topics. A very popular example is the field of computational fluid dynamics. Although most publications on DG are journal papers, the book of Hesthaven and Warburton [35] gives a comprehensive study of the DG method.

DG is a local method which makes it very flexible in terms of *hp*-adaptivity and non-conformal grids [36]-[37]. Additionally, the associated mass matrix is strictly block diagonal due to the local formulation and allows an efficient explicit time integration which is not the case for continuous finite element method (FEM) in general. One of the drawbacks is the increasing amount of discrete unknowns that logically arise due to the discontinuity between two elements.

[2] The term numerical flux will be explained later.

We now want to apply the DG method to system (33). This is done in the following steps. Defining a weak formulation, choosing an appropriate space for the basis functions and eventually evaluating the resulting integrals. Although the following derivations are done with scalar test functions (as used in the implementation), we will use vectorial test functions for the subsequent stability analysis. Indeed, the equivalence of both formulations is guaranteed and this choice is only made for the sake of clarity.

3.2 Weak formulation

The weak formulation of system (33) is derived in the following. First, weak differential operators are defined and a polynomial ansatz space, subsequently. By taking the ansatz space as a basis for the approximation of the field quantities and as a basis for the test functions, the resulting integrals of the weak operators are evaluated. Again, we want to emphasize that the local polynomials cause the main difference between the continuous FEM and the DG approach.

3.2.1 Weak operators

The weak formulation of a differential operator reduces the required regularity of the field quantity. For the following derivations, we will denote an arbitrary vectorial field by $\mathbf{A} : \mathbb{R}^3 \times \mathbb{R} \mapsto \mathbb{R}^3$ and scalar fields by $\phi, \psi : \mathbb{R}^3 \times \mathbb{R} \mapsto \mathbb{R}$. Taking the well known vector analytical identity

$$\nabla \times (\phi \mathbf{A}) = \phi \nabla \times \mathbf{A} - \mathbf{A} \times \nabla \phi, \tag{58}$$

and integrating over an arbitrary three dimensional domain Ω yields

$$\int_\Omega \nabla \times \mathbf{A}\phi \ \mathrm{d}^3\mathbf{r} = \int_\Omega \nabla \times (\phi \mathbf{A}) \ \mathrm{d}^3\mathbf{r} + \int_\Omega \mathbf{A} \times \nabla \phi \ \mathrm{d}^3\mathbf{r}, \tag{59}$$

and together with Stoke's theorem

$$\int_\Omega \nabla \times \mathbf{A}\phi \ \mathrm{d}^3\mathbf{r} = \int_\Omega \mathbf{A} \times \nabla \phi \ \mathrm{d}^3\mathbf{r} + \int_{\partial\Omega} (\mathbf{n} \times \mathbf{A})\phi \ \mathrm{d}^2\mathbf{r}. \tag{60}$$

Proceeding analogously for the grad operator leads to

$$\nabla(\phi\psi) = \phi \nabla \psi + \psi \nabla \phi, \tag{61}$$

integrating over Ω

$$\int_\Omega \nabla\psi\phi \ \mathrm{d}^3\mathbf{r} = \int_\Omega \nabla(\phi\psi) \ \mathrm{d}^3\mathbf{r} - \int_\Omega \psi\nabla\phi \ \mathrm{d}^3\mathbf{r}, \tag{62}$$

and together with the gradient theorem

$$\int_\Omega \nabla\psi\phi \ \mathrm{d}^3\mathbf{r} = -\int_\Omega \psi\nabla\phi \ \mathrm{d}^3\mathbf{r} + \int_{\partial\Omega} \phi\psi\mathbf{n} \ \mathrm{d}^2\mathbf{r}. \tag{63}$$

Finally, the weak div is given in (66) by

$$\nabla\cdot(\phi\mathbf{A}) = \phi\nabla\cdot\mathbf{A} + \mathbf{A}\cdot\nabla\phi, \tag{64}$$

with the integration over Ω

$$\int_\Omega \nabla\cdot\mathbf{A}\phi \ \mathrm{d}^3\mathbf{r} = \int_\Omega \nabla\cdot(\phi\mathbf{A}) \ \mathrm{d}^3\mathbf{r} - \int_\Omega \mathbf{A}\nabla\phi \ \mathrm{d}^3\mathbf{r}, \tag{65}$$

and the use of Gauss' theorem gives

$$\int_\Omega \nabla\cdot\mathbf{A}\phi \ \mathrm{d}^3\mathbf{r} = -\int_\Omega \mathbf{A}\cdot\nabla\phi \ \mathrm{d}^3\mathbf{r} + \int_{\partial\Omega} \phi\mathbf{A}\cdot\mathbf{n} \ \mathrm{d}^2\mathbf{r}, \tag{66}$$

where we claim $\mathbf{A}$, ψ, and ϕ sufficiently regular. The weak formulation of the hydrodynamic fluid model reads

$$\int_\Omega \mathbf{H}\times\nabla\phi \ \mathrm{d}^3\mathbf{r} + \int_{\partial\Omega} \phi(\mathbf{n}\times\mathbf{H}) \ \mathrm{d}^2\mathbf{r} = \partial_t \int_\Omega \varepsilon_0\varepsilon_\infty\mathbf{E}\phi \ \mathrm{d}^3\mathbf{r} + \int_\Omega \mathbf{J}\phi \ \mathrm{d}^3\mathbf{r}, \tag{67a}$$

$$\int_\Omega \mathbf{E}\times\nabla\phi \ \mathrm{d}^3\mathbf{r} + \int_{\partial\Omega} \phi(\mathbf{n}\times\mathbf{E}) \ \mathrm{d}^2\mathbf{r} = -\partial_t \int_\Omega \mu_0\mathbf{H}\phi \ \mathrm{d}^3\mathbf{r}, \tag{67b}$$

for the Maxwell part, and for the hydrodynamic contribution

$$-\int_\Omega Q\nabla\phi \ \mathrm{d}^3\mathbf{r} + \int_{\partial\Omega} \phi Q\mathbf{n} \ \mathrm{d}^2\mathbf{r} = \partial_t \int_\Omega \frac{1}{\beta^2}\mathbf{J}\phi \ \mathrm{d}^3\mathbf{r} + \int_\Omega \frac{\gamma}{\beta^2}\mathbf{J}\phi \ \mathrm{d}^3\mathbf{r} - \int_\Omega \frac{\varepsilon_0\omega_p^2}{\beta^2}\mathbf{E}\phi \ \mathrm{d}^3\mathbf{r}, \tag{67c}$$

$$-\int_\Omega \mathbf{J}\cdot\nabla\phi \ \mathrm{d}^3\mathbf{r} + \int_{\partial\Omega} \phi\mathbf{J}\cdot\mathbf{n} \ \mathrm{d}^2\mathbf{r} = \partial_t \int_\Omega Q\phi \ \mathrm{d}^3\mathbf{r}. \tag{67d}$$

Here, we assume $\beta \neq 0$. Further, the test function should provide sufficient regularity, for example $\phi \in \mathsf{H}^1(\Omega)$. For the field quantities $\mathbf{E}, \mathbf{H}, \mathbf{J}$ and Q we assume a functional space $\mathcal{V}$ with sufficient regularity.

3.2.2 Polynomial ansatz space

Spatial discretization with the DG method requires or yields from a special choice of polynomial basis functions. The main difference between continuous FEM and DG is the absolutely local basis functions that are nonzero for one element only. In other words, each finite element, provides a set of basis functions and does not overlap with its neighbors. Due to the latter mentioned property, continuity of the fields is not enforced and discontinuities at the cell interfaces may arise. The treatment of those discontinuities provides an additional parameter for the design of the final algorithm. As we will see later, the discontinuities are only important for the surface integrals in (67) and are modeled by introducing numerical fluxes.

Depending on the chosen mesh, different polynomial bases are possible and more or less convenient. For instance, Legendre polynomials are one possibility for hexahedral meshes [38]. In our case, a tetrahedral mesh is used in combination with Lagrange polynomials. However, the actual polynomial basis is not of high importance at the moment since the following derivations are done for general meshes and basis functions. Nevertheless, it is necessary to be aware of the local basis $\mathcal{V}_i^p$ for each subspace i.e. mesh cell Ω_i. This basis depends on a characteristic mesh size h of each mesh. The complete computational domain is thus

$$\Omega = \bigcup_{\forall i \in \mathcal{N}_\Omega} \Omega_i, \tag{68}$$

with

$$s_{iq} = \Omega_i \cap \Omega_q, \quad \forall i, q \in \mathcal{N}_\Omega, \tag{69}$$

where $\mathcal{N}_\Omega$ is the set of element indices of the subdivision of Ω and element i and q are assumed to be neighbors. Figure 5 illustrates one mesh cell Ω_i for a hexahedral mesh. According to the upper arguments, the ansatz space is defined as

$$\mathcal{V}^p(\Omega) := \left\{ v \in \mathcal{L}^2(\Omega),\, v|_{\Omega_i} \in \mathcal{P}_p(\Omega_i),\ \forall i \in \mathcal{N}_\Omega \right\}, \tag{70}$$

where $\mathcal{P}_p(\Omega_i)$ is the space of polynomials of maximum degree p on Ω_i. Choosing the basis functions ϕ_{ij}, $\mathcal{V}^p(\Omega)$ can be interpreted as

$$\mathcal{V}^p(\Omega) = \text{span}\left[\phi_{ij}(\mathbf{r}) : \begin{cases} \phi_j(\mathbf{r}), & \mathbf{r} \in \Omega_i \\ 0, & \mathbf{r} \notin \Omega_i \end{cases},\ \forall i \in \mathcal{N}_\Omega \right]. \tag{71}$$

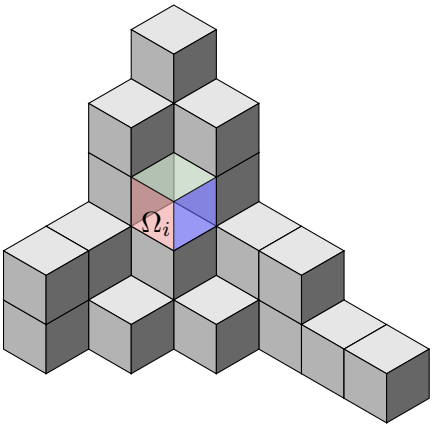

Figure 5: The colored cube illustrates one finite element in the spatial domain. All basis and test functions ϕ_{ij} from an element Ω_i are only non-zero on Ω_i.

Here, ϕ_{ij} denotes the basis function associated to the degree of freedom j of element i.

3.2.3 Semi-discrete weak form

Having a look at system (67), we remark that all spatial derivatives have been taken away from the unknowns and affect the test functions ϕ only. Together with the previously defined ansatz space the field quantities can be expressed as

$$\mathbf{A}|_{\Omega_i}(t) = \mathbf{A}_i(t) := \sum_{u=1}^{3}\sum_{j=1}^{P_i} A_{ij}^u(t)\phi_{ij}\mathbf{e}_u, \quad \mathbf{A} \in \{\mathbf{H}, \mathbf{E}, \mathbf{J}\} \tag{72a}$$

$$Q|_{\Omega_i}(t) = Q_i(t) := \sum_{j=1}^{P_i} Q_{ij}(t)\phi_{ij}, \tag{72b}$$

where u is the spatial dimension and P_i the number of degrees of freedom (DoFs) for the i-th element. A finite element Ω_i is illustrated in Figure 5. The expressions in (72) are polynomial approximations on each cell. Due to the h dependency of $\mathcal{V}_i^p$, those fields implicitly depend on h, also. As it is shown below, the results can be expressed as a matrix vector multiplication of a certain matrix with a vector that contains the DoFs. The final weak formulation now reads: for all i, j, k, and u find

$E^u_{ij}, H^u_{ij}, J^u_{ij}, Q_{ij}$ such that

$$\int_{\Omega_i} \mathbf{H}_i \times \nabla\phi_{ik} \, \mathrm{d}^3\mathbf{r} + \int_{\partial\Omega_i} \phi_{ik}(\mathbf{n} \times \mathbf{H}_i^\star) \, \mathrm{d}^2\mathbf{r} = \partial_t \int_{\Omega_i} \varepsilon_0\varepsilon_\infty \mathbf{E}_i\phi_{ik} \, \mathrm{d}^3\mathbf{r} + \int_{\Omega_i} \mathbf{J}_i\phi_{ik} \, \mathrm{d}^3\mathbf{r}, \tag{73a}$$

$$\int_{\Omega_i} \mathbf{E}_i \times \nabla\phi_{ik} \, \mathrm{d}^3\mathbf{r} + \int_{\partial\Omega_i} \phi_{ik}(\mathbf{n} \times \mathbf{E}_i^\star) \, \mathrm{d}^2\mathbf{r} = -\partial_t \int_{\Omega_i} \mu_0 \mathbf{H}_i\phi_{ik} \, \mathrm{d}^3\mathbf{r}, \tag{73b}$$

for the Maxwell part and for the hydrodynamic contribution

$$-\int_{\Omega_i} Q_i \nabla\phi_{ik} \, \mathrm{d}^3\mathbf{r} + \int_{\partial\Omega_i} \phi_{ik} Q_i^\star \mathbf{n} \, \mathrm{d}^2\mathbf{r} = \partial_t \int_{\Omega_i} \frac{1}{\beta^2} \mathbf{J}_i\phi_{ik} \, \mathrm{d}^3\mathbf{r} + \int_{\Omega_i} \frac{\gamma}{\beta^2} \mathbf{J}_i\phi_{ik} \, \mathrm{d}^3\mathbf{r} - \int_{\Omega_i} \frac{\varepsilon_0\omega_p^2}{\beta^2} \mathbf{E}_i\phi_{ik} \, \mathrm{d}^3\mathbf{r}, \tag{73c}$$

$$-\int_{\Omega_i} \mathbf{J}_i \cdot \nabla\phi_{ik} \, \mathrm{d}^3\mathbf{r} + \int_{\partial\Omega_i} \phi_{ik} \mathbf{J}_i^\star \cdot \mathbf{n} \, \mathrm{d}^2\mathbf{r} = \partial_t \int_{\Omega_i} Q_i\phi_{ik} \, \mathrm{d}^3\mathbf{r}, \tag{73d}$$

is fulfilled. Here, we used the relation on Ω_i

$$\phi_{ij}\phi_{lk} = \begin{cases} \phi_{ij}\phi_{ik}, & i = l \\ 0, & i \neq l \end{cases}, \tag{74}$$

yielding from (71). The additional $(\,\cdot\,)^\star$ emphasizes the field values on the boundary $\partial\Omega_i$ and will become clearer when the flux matrices are evaluated. We want to use this notation because of the possible discontinuity between two elements. Indeed, the field value at the interface is not naturally defined.

3.3 Mass matrix

Let us now have a look at the integrals of the form

$$\int_{\Omega_i} \alpha \sum_{u=1}^{3} \sum_{j=1}^{P_i} A^u_{ij}\phi_{ij}\mathbf{e}_u\phi_{ik} \, \mathrm{d}^3\mathbf{r}, \tag{75}$$

where α is a generalized material parameter. Rewriting this expression in matricial form we define a vector containing DoFs by means of $\mathbf{A_i} \in \mathbb{R}^{3P_i \times 1}$ with $\{\mathbf{A_i}\}_{j+u\cdot P_i} =$

A_{ij}^u. This leads to the definition of

$$(\mathbb{M}_i^\alpha)_{kj}^u := \int_{\Omega_i} \alpha \phi_{ij} \phi_{ik} \, \mathrm{d}^3\mathbf{r}, \tag{76}$$

$$\mathbb{M}_i^\alpha = \mathrm{diag}\left\{(\mathbb{M}_i^\alpha)^{u_1}, (\mathbb{M}_i^\alpha)^{u_2}, (\mathbb{M}_i^\alpha)^{u_3}\right\}, \in \mathbb{R}^{3P_i \times 3P_i}. \tag{77}$$

This matrix is called *mass matrix* and shows block diagonality in the DG framework. Block diagonality is a very important property that makes explicit time domain integration computationally affordable and is one of the main advantages of the DG method. Classical FEM do not provide this property and are therefore numerically more expensive for transient electromagnetic problems in time domain. In our case, we furthermore assume that the material parameters are constant per cell. Thus (77) can be rewritten in the following form

$$\mathbb{M}_i = \alpha \, \mathrm{diag}\left\{(\mathbb{M}_i)^{u_1}, (\mathbb{M}_i)^{u_2}, (\mathbb{M}_i)^{u_3}\right\}, \in \mathbb{R}^{3P_i \times 3P_i}. \tag{78}$$

3.4 Stiffness matrix

While the mass matrix does not involve any spatial derivatives, the stiffness matrix carries the *inner* part of the original differential operators' weak form. In other words, the spatial derivative is split into an *inner stiffness* and *outer flux* matrix. For the weak curl operator, the stiffness part reads

$$\int_{\Omega_i} \mathbf{A}_i \times \nabla \phi_{ik} \, \mathrm{d}^3\mathbf{r} = \int_{\Omega_i} \sum_{u=1}^{3} \sum_{j=1}^{P_i} A_{ij}^u \phi_{ij} \mathbf{e}_u \times \nabla \phi_{ik} \, \mathrm{d}^3\mathbf{r}, \tag{79}$$

$$(\mathbb{S}_i)_{kj}^u := \int_{\Omega_i} \phi_{ij} \mathbf{e}_u \times \nabla \phi_{ik} \, \mathrm{d}^3\mathbf{r}, \tag{80}$$

$$\mathbb{S}_i = \mathrm{diag}\left\{(\mathbb{S}_i)^{u_1}, (\mathbb{S}_i)^{u_2}, (\mathbb{S}_i)^{u_3}\right\} \in \mathbb{R}^{3P_i \times 3P_i}. \tag{81}$$

Analogously for the grad term

$$\begin{aligned}\int_{\Omega_i} Q_i \nabla\phi_{ik}\ \mathrm{d}^3\mathbf{r} &= \int_{\Omega_i} \sum_{j=1}^{P_i} Q_{ij}\phi_{ij}\nabla\phi_{ik}\ \mathrm{d}^3\mathbf{r}, \\ &= \sum_{j=1}^{P_i} Q_{ij} \int_{\Omega_i} \phi_{ij}\nabla\phi_{ik}\ \mathrm{d}^3\mathbf{r},\end{aligned} \tag{82}$$

$$(\mathbb{G}_i)^u_{kj} := \int_{\Omega_i} \phi_{ij}\partial_u\phi_{ik}\ \mathrm{d}^3\mathbf{r}, \tag{83}$$

$$\mathbb{G}_i := \begin{pmatrix} (\mathbb{G}_i)^{u_1} \\ (\mathbb{G}_i)^{u_2} \\ (\mathbb{G}_i)^{u_3} \end{pmatrix} \in \mathbb{R}^{3P_i \times P_i}, \tag{84}$$

and finally for the div term

$$\begin{aligned}\int_{\Omega_i} \mathbf{J}_i \cdot \nabla\phi_{ik}\ \mathrm{d}^3\mathbf{r} &= \int_{\Omega_i} \sum_{u=1}^{3}\sum_{j=1}^{P_i} J^u_{ij}\phi_{ij}\mathbf{e}_u \cdot \nabla\phi_{ik}\ \mathrm{d}^3\mathbf{r}, \\ &= \sum_{u=1}^{3}\sum_{j=1}^{P_i} J^u_{ij}\mathbf{e}_u \cdot \int_{\Omega_i} \phi_{ij}\nabla\phi_{ik}\ \mathrm{d}^3\mathbf{r},\end{aligned} \tag{85}$$

$$(\mathbb{D}_i)^u_{kj} := \int_{\Omega_i} \phi_{ij}\partial_u\phi_{ik}\ \mathrm{d}^3\mathbf{r}, \tag{86}$$

$$\mathbb{D}_i := \begin{pmatrix} (\mathbb{D}_i)^{u_1} & (\mathbb{D}_i)^{u_2} & (\mathbb{D}_i)^{u_3} \end{pmatrix} \in \mathbb{R}^{P_i \times 3P_i}. \tag{87}$$

3.5 Flux matrix

One of the special but also crucial points for the DG method is the definition of the field quantity at the boundary of neighboring cells. Centered fluxes, for example, usually have the advantage to be energy preserving. Those fluxes average the field quantities of the contributing elements at the cell interface s_{iq} pointing from element i to element q according to (88) and Figure 6 and 7. Another possible approach are upwind fluxes analogously to finite volume schemes where the boundary value is defined with respect to wave propagation direction. These fluxes cause numerical dissipation while spurious solutions are damped in time. Many different fluxes are generally imaginable and a few of them are analyzed in [35]-[38]. Throughout this work we will only consider centered fluxes (also known as centered DG). Defining

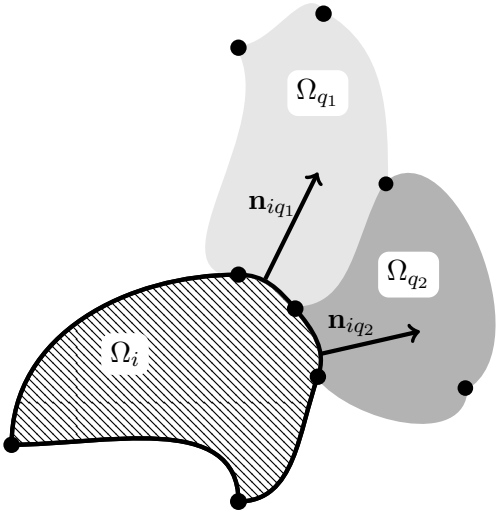

Figure 6: Interface in between two neighbor elements with respect to the cell Ω_i. The surface normals $\mathbf{n}_{iq}$ point orthogonally to the boundary $\partial\Omega_i$.

the average

$$\mathbf{A}_i^\star = \frac{\mathbf{A}_i + \mathbf{A}_q}{2}, \tag{88}$$

on the interface between element i and q of the general field $\mathbf{A}$, yields for Ampère's and Faraday's laws

$$\begin{aligned}\int_{\partial\Omega_i} \phi_{ik}(\mathbf{n}\times\mathbf{A}_i^\star)\,\mathrm{d}^2\mathbf{r} &= \sum_{q=1}^{N_q^i}\int_{s_{iq}} \phi_{ik}\left(\mathbf{n}_{iq}\times\frac{\mathbf{A}_i+\mathbf{A}_q}{2}\right)\,\mathrm{d}^2\mathbf{r}\\ &= \frac{1}{2}\sum_{q=1}^{N_q^i}\int_{s_{iq}}\left[\underbrace{\phi_{ik}\left(\mathbf{n}_{iq}\times\mathbf{A}_i\right)}_{\text{self flux}}+\underbrace{\phi_{ik}\left(\mathbf{n}_{iq}\times\mathbf{A}_q\right)}_{\text{neighbor flux}}\right]\,\mathrm{d}^2\mathbf{r},\end{aligned} \tag{89}$$

where s_{iq} is the surface shared by element [3] i and q with

$$\partial\Omega_i = \bigcup_{q=1}^{N_q^i} s_{iq}, \tag{90}$$

[3] Only conformal grids are considered.

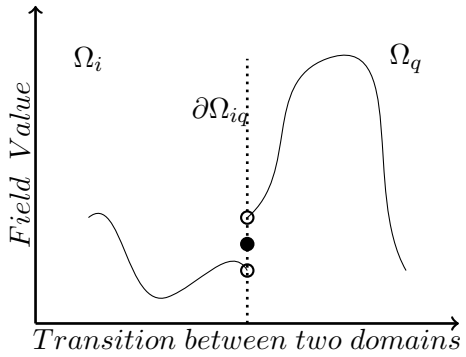

Figure 7: A discontinuity can appear at any shared boundary of Ω_i and Ω_j. The not filled circles are the fields of each cell at the interface while the 'global' field value is marked by the black dot. This sketch illustrates only the principle without any coordinate axis or determined dimensions.

with the number of neighbors N_q^i. Let us derive the matrix form of the self flux [4]

$$\begin{aligned}
&\frac{1}{2}\sum_{q=1}^{N_q^i}\int_{s_{iq}}\sum_{u=1}^{3}\phi_{ik}\left(\mathbf{n}_{iq}\times\mathbf{e}_u\sum_{j=1}^{N_i}A_{ij}^u\phi_{ij}\right)\ \mathrm{d}^2\mathbf{r}\\
=&\frac{1}{2}\sum_{q=1}^{N_q^i}\int_{s_{iq}}\sum_{u=1}^{3}\sum_{j=1}^{N_i}A_{ij}^u\phi_{ik}\left(\mathbf{n}_{iq}\times\mathbf{e}_u\phi_{ij}\right)\ \mathrm{d}^2\mathbf{r},
\end{aligned} \tag{91}$$

$$\begin{aligned}
\left(\left(\mathbb{F}_{\mathsf{curl}}\right)_{iq}^{s}\right)_{jk}^{u} &= \int_{s_{iq}}\phi_{ik}\phi_{ij}\left(\mathbf{n}_{iq}\times\mathbf{e}_u\right)\ \mathrm{d}^2\mathbf{r},\\
\left(\left(\mathbb{F}_{\mathsf{curl}}\right)_{iq}^{n}\right)_{jk}^{u} &= \int_{s_{iq}}\phi_{ik}\phi_{qj}\left(\mathbf{n}_{iq}\times\mathbf{e}_u\right)\ \mathrm{d}^2\mathbf{r}.
\end{aligned} \tag{92}$$

Here, $\left(\mathbb{F}_{\mathsf{curl}}\right)_{iq}^{s}$ represents the contribution yielding from the element itself while the contribution of each neighboring element is provided by $\left(\mathbb{F}_{\mathsf{curl}}\right)_{iq}^{n}$. N_i is the number of DoFs per face. The boundary integral for Q has a different structure and leads

[4] The derivation of the neighbor flux is then similar.

with the central flux to

$$\begin{aligned}\int\limits_{\partial\Omega_i} \phi_{ik} Q_i^\star \mathbf{n}\, \mathrm{d}^2\mathbf{r} &= \sum_{q=1}^{N_q^i} \int\limits_{s_{iq}} \phi_{ik} \left(\frac{Q_i + Q_q}{2}\right) \mathbf{n}_{iq}\, \mathrm{d}^2\mathbf{r}, \\ &= \underbrace{\frac{1}{2} \sum_{q=1}^{N_q^i} \sum_{j=1}^{N_i} Q_{ij} \int\limits_{s_{iq}} \phi_{ik}\phi_{ij}\mathbf{n}_{iq}\, \mathrm{d}^2\mathbf{r}}_{\text{self flux}} \\ &\quad + \underbrace{\frac{1}{2} \sum_{q=1}^{N_q^i} \sum_{j=1}^{N_q} Q_{qj} \int\limits_{s_{iq}} \phi_{ik}\phi_{qj}\mathbf{n}_{iq}\, \mathrm{d}^2\mathbf{r}}_{\text{neighbor flux}}.\end{aligned} \tag{93}$$

continuing in the same manner as before yields

$$\begin{aligned}\left((\mathbb{F}_{\mathsf{grad}}\,)_{iq}^s\right)_{jk} &= \int\limits_{s_{iq}} \phi_{ik}\phi_{ij}\mathbf{n}_{iq}\, \mathrm{d}^2\mathbf{r}, \\ \left((\mathbb{F}_{\mathsf{grad}}\,)_{iq}^n\right)_{jk} &= \int\limits_{s_{iq}} \phi_{ik}\phi_{qj}\mathbf{n}_{iq}\, \mathrm{d}^2\mathbf{r}.\end{aligned} \tag{94}$$

Evaluating the flux terms for the polarization current leads to

$$\begin{aligned}\int\limits_{\partial\Omega_i} \phi_{ik} \mathbf{J}_i^\star \cdot \mathbf{n}\, \mathrm{d}^2\mathbf{r} &= \sum_{q=1}^{N_q^i} \int\limits_{s_{iq}} \phi_{ik} \left(\frac{\mathbf{J}_i + \mathbf{J}_q}{2}\right) \cdot \mathbf{n}_{iq}\, \mathrm{d}^2\mathbf{r}, \\ &= \underbrace{\frac{1}{2} \sum_{q=1}^{N_q^i} \sum_{u=1}^{3} \sum_{j=1}^{N_i} J_{ij}^u \int\limits_{s_{iq}} \phi_{ik}\phi_{ij}\mathbf{e}_u\mathbf{n}_{iq}\, \mathrm{d}^2\mathbf{r}}_{\text{self flux}} \\ &\quad + \underbrace{\frac{1}{2} \sum_{q=1}^{N_q^i} \sum_{u=1}^{3} \sum_{j=1}^{N_i} J_{qj}^u \int\limits_{s_{iq}} \phi_{ik}\phi_{qj}\mathbf{e}_u\mathbf{n}_{iq}\, \mathrm{d}^2\mathbf{r}}_{\text{neighbor flux}},\end{aligned} \tag{95}$$

and thus for the matrix notation

$$\begin{aligned}\left((\mathbb{F}_{\mathsf{div}}\,)^{s}_{iq}\right)^{u}_{jk} &= \int\limits_{s_{iq}} \phi_{ik}\phi_{ij}\mathbf{e}_u\mathbf{n}_{iq}\;\mathrm{d}^2\mathbf{r},\\ \left((\mathbb{F}_{\mathsf{div}}\,)^{n}_{iq}\right)^{u}_{jk} &= \int\limits_{s_{iq}} \phi_{ik}\phi_{qj}\mathbf{e}_u\mathbf{n}_{iq}\;\mathrm{d}^2\mathbf{r}.\end{aligned} \tag{96}$$

From now on, the flux matrices acting on the electric and magnetic fields will be denoted by $\mathbb{F}_{\mathsf{curl}}$, those which act on the polarization charge density by $\mathbb{F}_{\mathsf{grad}}$ and finally for the current density $\mathbb{F}_{\mathsf{div}}$.

3.6 Semi-discrete stability

In order to study semi-discrete stability, it is more convenient to use a formulation with vectorial basis functions. Both formulations are equivalent if the vectorial basis is chosen as

$$\phi^{u}_{ij} := \phi_{ij}\mathbf{e}_u. \tag{97}$$

Defining a notation for the average on the interface between element i and q of a field quantity $\mathbf{A}$ by means of

$$\{\mathbf{A}\}_{iq} := \left.\frac{\mathbf{A}_i + \mathbf{A}_q}{2}\right|_{s_{iq}}, \tag{98}$$

the weak form with vectorial test functions reads

$$\begin{aligned}
\varepsilon_0\varepsilon_\infty\partial_t \int_{\Omega_i} \mathbf{E}_i\cdot\phi_{i\mathbf{E}}\,\mathrm{d}^3\mathbf{r} &= \int_{\Omega_i} \mathbf{H}_i\cdot(\nabla\times\phi_{i\mathbf{E}})\,\mathrm{d}^3\mathbf{r} \\
&\quad - \sum_{q=1}^{N_q}\int_{s_{iq}} \phi_{i\mathbf{E}}\cdot\left(\{\mathbf{H}\}_{iq}\times\mathbf{n}_{iq}\right)\,\mathrm{d}^2\mathbf{r} \qquad (99a)\\
&\quad - \int_{\Omega_i}\mathbf{J}_i\cdot\phi_{i\mathbf{E}}\,\mathrm{d}^3\mathbf{r}, \\
\mu_0\partial_t \int_{\Omega_i} \mathbf{H}_i\cdot\phi_{i\mathbf{H}}\,\mathrm{d}^3\mathbf{r} &= -\int_{\Omega_i} \mathbf{E}_i\cdot(\nabla\times\phi_{i\mathbf{H}})\,\mathrm{d}^3\mathbf{r} \\
&\quad + \sum_{q=1}^{N_q}\int_{s_{iq}} \phi_{i\mathbf{H}}\cdot\left(\{\mathbf{E}\}_{iq}\times\mathbf{n}_{iq}\right)\,\mathrm{d}^2\mathbf{r}, \qquad (99b)\\
\partial_t \int_{\Omega_i} \mathbf{J}_i\cdot\phi_{i\mathbf{J}}\,\mathrm{d}^3\mathbf{r} &= -\beta^2\int_{\Omega_i} Q_i\nabla\cdot\phi_{i\mathbf{J}}\,\mathrm{d}^3\mathbf{r} \\
&\quad + \beta^2\sum_{q=1}^{N_q}\int_{s_{iq}}\{Q\}_{iq}\,\phi_{i\mathbf{J}}\cdot\mathbf{n}_{iq}\,\mathrm{d}^2\mathbf{r} \qquad (99c)\\
&\quad + \omega_p^2\varepsilon_0\int_{\Omega_i}\mathbf{E}_i\cdot\phi_{i\mathbf{J}}\,\mathrm{d}^3\mathbf{r} - \gamma\int_{\Omega_i}\mathbf{J}_i\cdot\phi_{i\mathbf{J}}\,\mathrm{d}^3\mathbf{r}, \\
\partial_t \int_{\Omega_i} Q_i\phi_{iQ}\,\mathrm{d}^3\mathbf{r} &= -\int_{\Omega_i}\mathbf{J}_i\cdot\nabla\phi_{iQ}\,\mathrm{d}^3\mathbf{r} \qquad (99d)\\
&\quad + \sum_{q=1}^{N_q}\int_{s_{iq}}\phi_{iQ}\,\{\mathbf{J}\}_{iq}\cdot\mathbf{n}_{iq}\,\mathrm{d}^2\mathbf{r}. \qquad (99e)
\end{aligned}$$

Here, $\{\phi_{i\mathbf{E}},\phi_{i\mathbf{H}},\phi_{i\mathbf{J}}\}:\mathbb{R}^3\mapsto\mathbb{R}^3$ and $\phi_{iQ}:\mathbb{R}^3\mapsto\mathbb{R}$ are appropriate test functions. Testing (99) with

$$\{\phi_{i\mathbf{E}},\phi_{i\mathbf{H}},\phi_{i\mathbf{J}},\phi_{iQ}\}=\{\mathbf{E}_i,\mathbf{H}_i,\mathbf{J}_i,Q_i\}\,, \qquad (100)$$

and defining the semi-discrete energy on each element Ω_i analogously to the analytical definition in (43) as

$$\mathcal{E}(t)_i := \frac{1}{2}\left[\mu_0\omega_p^2\varepsilon_0\|\mathbf{H}_i\|_{\Omega_i}^2+\varepsilon_\infty\varepsilon_0^2\omega_p^2\|\mathbf{E}_i\|_{\Omega_i}^2+\|\mathbf{J}_i\|_{\Omega_i}^2+\beta^2\|Q_i\|_{\Omega_i}^2\right],$$

leads to the power per cell

$$\begin{aligned}\partial_t \mathcal{E}(t)_i = \omega_p^2 \varepsilon_0 \sum_{q=1}^{N_q} \int_{s_{iq}} \left[\mathbf{H}_i \cdot \left(\{\mathbf{E}\}_{iq} \times \mathbf{n}_{iq} \right) - \mathbf{E}_i \cdot \left(\{\mathbf{H}\}_{iq} \times \mathbf{n}_{iq} \right) \right] \, \mathrm{d}^2\mathbf{r} \\ + \omega_p^2 \varepsilon_0 \int_{\Omega_i} \left[\mathbf{E}_i \cdot (\nabla \times \mathbf{H}_i) - \mathbf{H}_i \cdot (\nabla \times \mathbf{E}_i) \right] \, \mathrm{d}^3\mathbf{r} \\ + \beta^2 \sum_{q=1}^{N_q} \left(\{Q\}_{iq} \mathbf{J}_i \cdot \mathbf{n}_{iq} + Q_i \{\mathbf{J}\}_{iq} \cdot \mathbf{n}_{iq} \right) \, \mathrm{d}^2\mathbf{r} \\ - \beta^2 \int_{\Omega_i} \nabla \cdot (Q_i \mathbf{J}_i) \, \mathrm{d}^3\mathbf{r} - \gamma \|\mathbf{J}_i\|_{\Omega_i}^2 .\end{aligned} \tag{101}$$

Integration by parts of one half of $\mathbf{E}_i \cdot (\nabla \times \mathbf{H}_i)$ and $\mathbf{H}_i \cdot (\nabla \times \mathbf{E}_i)$, respectively, and applying Gauss' theorem to the last integral of the div term yields

$$\begin{aligned}\partial_t \mathcal{E}(t)_i = \frac{1}{2} \omega_p^2 \varepsilon_0 \sum_{q=1}^{N_q} \int_{s_{iq}} \left[\mathbf{H}_i \cdot (\mathbf{E}_q \times \mathbf{n}_{iq}) - \mathbf{E}_i \cdot (\mathbf{H}_q \times \mathbf{n}_{iq}) \right] \, \mathrm{d}^2\mathbf{r} \\ + \beta^2 \sum_{q=1}^{N_q} \int_{s_{iq}} (Q_q \mathbf{J}_i \cdot \mathbf{n}_{iq} + Q_i \mathbf{J}_q \cdot \mathbf{n}_{iq}) \, \mathrm{d}^2\mathbf{r} - \gamma \|\mathbf{J}_i\|_{\Omega_i}^2 ,\end{aligned} \tag{102}$$

where $\| \cdot \|_{\Omega_i}$ denotes the $\mathcal{L}^2(\Omega)$ norm for $\Omega = \Omega_i$. Summing over all elements i and assuming a boundary value problem as presented in subsection 2.5.3, the total power reads

$$\partial_t \mathcal{E}(t) = -\gamma \|\mathbf{J}\|_{\Omega_i} . \tag{103}$$

Thus, the semi-discrete stability is guarantied and a decrease of energy is observed for lossy media. The term lossy refers here to the friction of electrons due to γ.

4 Time discretization with the leap-frog scheme

The DG method is used for the spatial discretization and leads to the system (73) of ODEs. These ODEs are still continuous in time where the time dependency appears in the fields $E_{ij}^u(t), H_{ij}^u(t), J_{ij}^u(t)$ and $Q_{ij}(t)$. Since our goal is the numerical solution of the entire system of PDEs, the time has to be discretized as well. In our case, we will introduce a staggered time grid where the electric field as well as the charge density are allocated on the primary grid and the magnetic field as well as the current density on the dual grid, respectively. The latter is shifted in time by $\frac{\Delta t}{2}$

with respect to the primary one. This approach was firstly proposed in the context of FDTD methods for Maxwell's equations in [39] and is also known as leap-frog scheme. Applying a second order leap-frog scheme to system (73) and using again vectorial test functions as in (99) leads to

$$\begin{aligned}\varepsilon_0\varepsilon_\infty \int_{\Omega_i} \frac{\mathbf{E}_i^{n+1}-\mathbf{E}_i^n}{\Delta t}\cdot\phi_{i\mathbf{E}} &= \int_{\Omega_i} \mathbf{H}_i^{n+\frac{1}{2}}\cdot(\nabla\times\phi_{i\mathbf{E}}) \\ &\quad - \sum_{q=1}^{N_q}\int_{s_{iq}} \phi_{i\mathbf{E}}\cdot\left(\left\{\mathbf{H}^{n+\frac{1}{2}}\right\}_{iq}\times\mathbf{n}_{iq}\right) - \int_{\Omega_i}\mathbf{J}_i^{n+\frac{1}{2}}\cdot\phi_{i\mathbf{E}},\end{aligned} \tag{104a}$$

$$\begin{aligned}\mu_0 \int_{\Omega_i} \frac{\mathbf{H}_i^{n+\frac{3}{2}}-\mathbf{H}_i^{n+\frac{1}{2}}}{\Delta t}\cdot\phi_{i\mathbf{H}} &= -\int_{\Omega_i} \mathbf{E}_i^{n+1}\cdot(\nabla\times\phi_{i\mathbf{H}}) \\ &\quad + \sum_{q=1}^{N_q}\int_{s_{iq}} \phi_{i\mathbf{H}}\cdot\left(\left\{\mathbf{E}^{n+1}\right\}_{iq}\times\mathbf{n}_{iq}\right),\end{aligned} \tag{104b}$$

$$\begin{aligned}\int_{\Omega_i} \frac{\mathbf{J}_i^{n+\frac{3}{2}}-\mathbf{J}_i^{n+\frac{1}{2}}}{\Delta t}\cdot\phi_{i\mathbf{J}} &= -\beta^2\int_{\Omega_i} Q_i^{n+1}\nabla\cdot\phi_{i\mathbf{J}} \\ &\quad + \beta^2\sum_{q=1}^{N_q}\int_{s_{iq}}\left\{Q^{n+1}\right\}_{iq}\phi_{i\mathbf{J}}\cdot\mathbf{n}_{iq} \\ &\quad + \omega_p^2\varepsilon_0\int_{\Omega_i}\mathbf{E}_i^{n+1}\cdot\phi_{i\mathbf{J}} - \gamma\int_{\Omega_i}\frac{\mathbf{J}_i^{n+\frac{3}{2}}+\mathbf{J}_i^{n+\frac{1}{2}}}{2}\cdot\phi_{i\mathbf{J}},\end{aligned} \tag{104c}$$

$$\int_{\Omega_i}\frac{Q_i^{n+1}-Q_i^n}{\Delta t}\phi_{iQ} = -\int_{\Omega_i}\mathbf{J}_i^{n+\frac{1}{2}}\cdot\nabla\phi_{iQ} + \sum_{q=1}^{N_q}\int_{s_{iq}}\phi_{iQ}\left\{\mathbf{J}^{n+\frac{1}{2}}\right\}_{iq}\cdot\mathbf{n}_{iq}. \tag{104d}$$

Here, all integrals over the domain Ω_i and $\partial\Omega_i$ are evaluated with respect to the measure $\mathrm{d}^3\mathbf{r}$ and $\mathrm{d}^2\mathbf{r}$, respectively. However, those measures are omitted in the following derivations for the sake of simplicity. Taking this fully-discrete scheme as a starting point, we would like to study the stability of this scheme. The latter is split into two parts; bound of the energy and positivity. Here, bound can be interpreted as an increase of the energy at each time step by means of the transition from t_n to t_{n+1} with $t_{n+1} = t_n + \Delta t$.

4.1 Bound of the fully-discrete energy

The evolution in time of the discrete energy is studied now. We will proceed in a similar way as for the continuous physics in (44). Naively defining $\mathcal{E}_i^{n+\frac{1}{2}}$ with some arbitrary coefficients for the energy norm by means of

$$\mathcal{E}_i^{n+\frac{1}{2}} := \frac{1}{2}\left[a\int_{\Omega_i}\mathbf{H}_i^{n+\frac{1}{2}}\cdot\mathbf{H}_i^{n+\frac{1}{2}} + b\int_{\Omega_i}\mathbf{E}_i^{n+1}\cdot\mathbf{E}_i^{n} + c\int_{\Omega_i}\mathbf{J}_i^{n+\frac{1}{2}}\cdot\mathbf{J}_i^{n+\frac{1}{2}} + d\int_{\Omega_i}Q_i^{n+1}\cdot Q_i^{n}\right], \tag{105}$$

and adapt these constants later in order to obtain the decrease of the discrete energy. Let us define an artificial time level for quantities allocated on the dual time grid e.g. $\mathbf{H}_i^{n+\frac{1}{2}}$ and $\mathbf{H}_i^{n+\frac{3}{2}}$ as

$$\mathbf{A}_i^{[n+1]} := \frac{\mathbf{A}_i^{n+\frac{3}{2}} + \mathbf{A}_i^{n+\frac{1}{2}}}{2}. \tag{106}$$

Using this definition together with the energy defined in (105), the energy difference between time step $n+\frac{3}{2}$ and $n+\frac{1}{2}$ reads

$$\begin{aligned}2\left(\mathcal{E}_i^{n+\frac{3}{2}} - \mathcal{E}_i^{n+\frac{1}{2}}\right) = {}& 2a\int_{\Omega_i}\left(\mathbf{H}_i^{n+\frac{3}{2}} - \mathbf{H}_i^{n+\frac{1}{2}}\right)\cdot\mathbf{H}_i^{[n+1]} \\ & + b\int_{\Omega_i}\left(\mathbf{E}_i^{n+2}\cdot\mathbf{E}_i^{n+1} - \mathbf{E}_i^{n+1}\cdot\mathbf{E}_i^{n}\right) \\ & + 2c\int_{\Omega_i}\left(\mathbf{J}_i^{n+\frac{3}{2}} - \mathbf{J}_i^{n+\frac{1}{2}}\right)\cdot\mathbf{J}_i^{[n+1]} \\ & + d\int_{\Omega_i}\left(Q_i^{n+2}\cdot Q_i^{n+1} - Q_i^{n+1}\cdot Q_i^{n}\right).\end{aligned} \tag{107}$$

With an appropriate choice of the test functions at the time level t_{n+1} and evaluating the equations of (104) at the time levels $t_{n+1}, t_{n+\frac{1}{2}}$ and $t_{n+\frac{3}{2}}$ according to

- (104a) at time $t_{n+\frac{1}{2}}$ and $t_{n+\frac{3}{2}}$ with $\mathbf{E}_i^{n+1}$,
- (104b) at time t_{n+1} with $\mathbf{H}_i^{[n+1]}$,
- (104c) at time t_{n+1} with $\mathbf{J}_i^{[n+1]}$,
- (104d) at time $t_{n+\frac{1}{2}}$ and $t_{n+\frac{3}{2}}$ with Q_i^{n+1},

(107) can be written as

$$\begin{aligned}
\mathcal{E}_i^{n+\frac{3}{2}} - \mathcal{E}_i^{n+\frac{1}{2}} = & \int\limits_{\Omega_i} \left[b\frac{\Delta t}{\varepsilon_0\varepsilon_\infty}\mathbf{H}_i^{[n+1]} \cdot \left(\nabla \times \mathbf{E}_i^{n+1}\right) - a\frac{\Delta t}{\mu_0}\mathbf{E}_i^{n+1} \cdot \left(\nabla \times \mathbf{H}_i^{[n+1]}\right)\right] \\
& + \sum_{q\in \mathsf{V}_i} \int\limits_{s_{iq}} \left[a\frac{\Delta t}{\mu_0}\mathbf{H}_i^{[n+1]} \cdot \left(\left\{\mathbf{E}^{n+1}\right\}_{iq} \times \mathbf{n}_{iq}\right) - \right. \\
& \qquad \left. b\frac{\Delta t}{\varepsilon_0\varepsilon_\infty}\mathbf{E}_i^{n+1} \cdot \left(\left\{\mathbf{H}^{[n+1]}\right\}_{iq} \times \mathbf{n}_{iq}\right)\right] \\
& - \int\limits_{\Omega_i} \left[c\Delta t\beta^2 Q_i^{n+1}\nabla\cdot\mathbf{J}_i^{[n+1]} + d\Delta t\mathbf{J}_i^{[n+1]}\cdot\nabla Q_i^{n+1}\right] \\
& + \Delta t \sum_{q\in \mathsf{V}_i} \int\limits_{s_{iq}} \left[c\beta^2 \left\{Q^{n+1}\right\}_{iq} \mathbf{J}_i^{[n+1]}\cdot\mathbf{n}_{iq} + d\, Q_i^{n+1}\left\{J^{n+1}\right\}_{iq}\cdot\mathbf{n}_{iq}\right] \\
& - b\frac{\Delta t}{\varepsilon_0\varepsilon_\infty}\int\limits_{\Omega_i} \mathbf{J}_i^{[n+1]}\cdot\mathbf{E}_i^{n+1} + c\omega_p^2\varepsilon_0\Delta t\int\limits_{\Omega_i}\mathbf{E}_i^{n+1}\cdot\mathbf{J}_i^{[n+1]} \\
& - c\gamma\Delta t\int\limits_{\Omega_i}\mathbf{J}_i^{[n+1]}\cdot\mathbf{J}_i^{[n+1]}.
\end{aligned}$$

Integrating by parts and setting $d = c\beta^2$ and $b = a\dfrac{\varepsilon_0\varepsilon_\infty}{\mu_0}$ finally leads to

$$\begin{aligned}
\mathcal{E}_i^{n+\frac{3}{2}} - \mathcal{E}_i^{n+\frac{1}{2}} = & \, a\frac{\Delta t}{\mu_0}\sum_{q\in \mathsf{V}_i}\int\limits_{s_{iq}} \left[\mathbf{H}_i^{[n+1]}\cdot\left(\frac{\mathbf{E}_q^{n+1}}{2}\times\mathbf{n}_{iq}\right) - \mathbf{E}_i^{n+1}\cdot\left(\frac{\mathbf{H}_q^{[n+1]}}{2}\times\mathbf{n}_{iq}\right)\right] \\
& + c\beta^2\Delta t\sum_{q\in \mathsf{V}_i}\int\limits_{s_{iq}}\left(Q_q^{n+1}\mathbf{J}_i^{[n+1]}\cdot\mathbf{n}_{iq} + Q_i^{n+1}\mathbf{J}_q^{[n+1]}\cdot\mathbf{n}_{iq}\right) \\
& - a\frac{\Delta t}{\mu_0}\int\limits_{\Omega_i}\mathbf{J}_i^{[n+1]}\cdot\mathbf{E}_i^{n+1} + c\omega_p^2\varepsilon_0\Delta t\int\limits_{\Omega_i}\mathbf{E}_i^{n+1}\cdot\mathbf{J}_i^{[n+1]} \\
& - c\gamma\Delta t\int\limits_{\Omega_i}\mathbf{J}_i^{[n+1]}\cdot\mathbf{J}_i^{[n+1]}.
\end{aligned}$$

Choosing the relation between a and c appropriately as $a = c\mu_0\omega_p^2\varepsilon_0$ and summing over all cells gives the total energy difference

$$\mathcal{E}^{n+\frac{3}{2}} - \mathcal{E}^{n+\frac{1}{2}} \leq -\gamma\Delta t\|\mathbf{J}\|_\Omega^2. \tag{108}$$

This is indeed a remarkable result because the purely centered DG scheme does not unphysically increase the energy for the coupled problem of Maxwell *together*

with the non-local dispersion model. Additionally, the scheme is energy preserving if electron collisions are neglected.

4.2 Positivity of the fully-discrete energy

We now want to study the positivity of the fully-discrete scheme. Therefore, we make some assumptions concerning the mesh properties. The underlying mesh is supposed to be tetrahedral and quasi-uniform. Defining the fully-discrete energy for each element i

$$\mathcal{E}_i^{n+\frac{1}{2}} := \frac{1}{2}\left[\mu_0\omega_p^2\varepsilon_0 \int\limits_{\Omega_i} \mathbf{H}_i^{n+\frac{1}{2}}\cdot\mathbf{H}_i^{n+\frac{1}{2}} + \varepsilon_\infty\varepsilon_0^2\omega_p^2 \int\limits_{\Omega_i} \mathbf{E}_i^{n+1}\cdot\mathbf{E}_i^{n} + \int\limits_{\Omega_i} \mathbf{J}_i^{n+\frac{1}{2}}\cdot\mathbf{J}_i^{n+\frac{1}{2}} + \beta^2 \int\limits_{\Omega_i} Q_i^{n+1}\cdot Q_i^{n}\right], \tag{109}$$

testing (104a) and (104d) with $\mathbf{E}_i^n$ and Q_i^n, respectively, gives

$$\int\limits_{\Omega_i} \mathbf{E}_i^{n+1}\cdot\mathbf{E}_i^{n} = \frac{\Delta t}{\varepsilon_0\varepsilon_\infty}\left[\int\limits_{\Omega_i} \mathbf{H}_i^{n+\frac{1}{2}}\cdot(\nabla\times\mathbf{E}_i^n) - \sum_{q=1}^{N_q}\int\limits_{s_{iq}} \mathbf{E}_i^n\cdot\left(\left\{\mathbf{H}^{n+\frac{1}{2}}\right\}_{iq}\times\mathbf{n}_{iq}\right) - \int\limits_{\Omega_i}\mathbf{J}_i^{n+\frac{1}{2}}\cdot\mathbf{E}_i^n\right] + \|\mathbf{E}_i^n\|_{\Omega_i}^2, \tag{110}$$

$$\int\limits_{\Omega_i} Q_i^{n+1}Q_i^n = \Delta t\left[-\int\limits_{\Omega_i}\mathbf{J}_i^{n+\frac{1}{2}}\cdot\nabla Q_i^n + \sum_{q=1}^{N_q}\int\limits_{s_{iq}} Q_i^n\left\{\mathbf{J}^{n+\frac{1}{2}}\right\}_{iq}\cdot\mathbf{n}_{iq}\right] + \|Q_i^n\|_{\Omega_i}^2. \tag{111}$$

We now have to plug these two expressions into the discrete energy given in (109). The following lemma linking the $\mathcal{L}^2(\Omega_i)$-norm of the differential operators applied to a vector field $\mathbf{A}$ and a scalar field Ψ, respectively with the field values' norm. These relations are very helpful for the following derivations concerning the positivity and bound of the discrete energy.

Lemma 2 *Let Ω_i be a mesh cell and h_i its size. Then, $\exists C \geq 0$ independent of h_i*

such that

$$\|\nabla \times \mathbf{A}\|_{\Omega_i} \leq \frac{C}{h_i}\|\mathbf{A}\|_{\Omega_i}, \tag{112}$$

$$\|\nabla \Psi\|_{\Omega_i} \leq \frac{C}{h_i}\|\Psi\|_{\Omega_i}, \tag{113}$$

$$\|\nabla \cdot \mathbf{A}\|_{\Omega_i} \leq \frac{C}{h_i}\|\mathbf{A}\|_{\Omega_i}, \tag{114}$$

$$\|\mathbf{A}\|_{s_{iq}} \leq \frac{C}{\sqrt{h_i}}\|\mathbf{A}\|_{\Omega_i}, \tag{115}$$

hold for $\mathbf{A}$ *and* ψ *polynomial in* Ω_i*. [40]*

With the relations provided by Lemma 2 and the Cauchy-Schwartz inequality, the following integral bounds can be derived. After some calculations, the final bounds read

$$\left| \int_{\Omega_i} \mathbf{A} \cdot (\nabla \times \mathbf{B}) + \mathbf{B} \cdot (\nabla \times \mathbf{A}) \right| \leq \frac{C}{h_i}\|\mathbf{A}\|_{\Omega_i}\|\mathbf{B}\|_{\Omega_i}, \tag{116}$$

$$\left| \int_{\Omega_i} \mathbf{A} \cdot \nabla \Psi + \Psi \nabla \cdot \mathbf{A} \right| \leq \frac{C}{h_i}\|\mathbf{A}\|_{\Omega_i}\|\Psi\|_{\Omega_i}, \tag{117}$$

$$\left| \int_{s_{iq}} \mathbf{A} \cdot (\mathbf{B} \times \mathbf{n}_{iq}) \right| \leq \frac{C}{h_i}\|\mathbf{A}\|_{\Omega_i}\|\mathbf{B}\|_{\Omega_i}, \tag{118}$$

$$\left| \int_{s_{iq}} \Psi \mathbf{A} \cdot \mathbf{n}_{iq} \right| \leq \frac{C}{h_i}\|\Psi\|_{\Omega_i}\|\mathbf{A}\|_{\Omega_i}, \tag{119}$$

$$\left| \int_{\Omega_i} \mathbf{A} \cdot \mathbf{B} \right| \leq \|\mathbf{A}\|_{\Omega_i}\|\mathbf{B}\|_{\Omega_i}. \tag{120}$$

In the following, the superscripts for the time level are neglected. The magnetic field $\mathbf{H}_i$ and the current density $\mathbf{J}_i$ are thus evaluated at the time $t_{n+\frac{1}{2}}$ while $\mathbf{E}_i$ and Q_i remain at t_n. Applying the latter integral bounds to (109) together with the classical inequality $ab \leq \frac{1}{2}(a^2 + b^2)$ and the assumption of a quasi-uniform mesh that allows the generalization of h_i to h with a readjustment of C [8], leads to the energy

at time $t_{n+\frac{1}{2}}$

$$\begin{aligned}
\mathcal{E}_i^{n+\frac{1}{2}} \geq\ & \|\mathbf{H}_i\|_{\Omega_i}^2 + \varepsilon_\infty \varepsilon_0^2 \omega_p^2 \|\mathbf{E}_i\|_{\Omega_i}^2 + \|\mathbf{J}_i\|_{\Omega_i}^2 + \beta^2 \|Q_i\|_{\Omega_i}^2 \\
& - \frac{\Delta t C \varepsilon_0 \omega_p^2}{4h} \left[\|\mathbf{E}_i\|_{\Omega_i}^2 + \|\mathbf{H}_i\|_{\Omega_i}^2 + \sum_{q \in \mathsf{V}_\mathsf{i}^\mathsf{int}} \left(\|\mathbf{E}_i\|_{\Omega_i}^2 + \|\mathbf{H}_q\|_{\Omega_q}^2 \right) \right. \\
& \left. + \sum_{q \in \mathsf{V}_\mathsf{i}^\mathsf{ext}} \left(\|\mathbf{E}_i\|_{\Omega_i}^2 + \|\mathbf{H}_i\|_{\Omega_i}^2 \right) + \frac{2h}{C} \left(\|\mathbf{E}_i\|_{\Omega_i}^2 + \|\mathbf{J}_i\|_{\Omega_i}^2 \right) \right] \\
& - \frac{\Delta t C \beta^2}{4h} \left[\|\mathbf{J}_i\|_{\Omega_i}^2 + \|Q\|_{\Omega_i}^2 + \sum_{q \in \mathsf{V}_\mathsf{i}^\mathsf{int}} \left(\|Q_i\|_{\Omega_i}^2 + \|\mathbf{J}_q\|_{\Omega_q}^2 \right) \right. \\
& \left. + \sum_{q \in \mathsf{V}_\mathsf{i}^\mathsf{ext}} \left(\|Q_i\|_{\Omega_i}^2 + \|\mathbf{J}_i\|_{\Omega_i}^2 \right) \right]. \qquad (121)
\end{aligned}$$

Here, we have split the set V_i of all interfaces of element i into two subsets $\mathsf{V}_\mathsf{i} = \mathsf{V}_\mathsf{i}^\mathsf{int} \cup \mathsf{V}_\mathsf{i}^\mathsf{ext}$ ($\overline{\mathsf{V}}_\mathsf{i}^\mathsf{int} \cap \overline{\mathsf{V}}_\mathsf{i}^\mathsf{ext} = \emptyset$) where $\mathsf{V}_\mathsf{i}^\mathsf{int}$ contains the inner interfaces and $\mathsf{V}_\mathsf{i}^\mathsf{ext}$ the interfaces that intersect with the boundary of the computational domain Ω. Summing over all cells together with the assumptions according to [8] and adjusting C yields

$$\begin{aligned}
\mathcal{E}^{n+\frac{1}{2}} \geq\ & \left[1 - \frac{C \Delta t \varepsilon_0 \omega_p^2}{h} \left(2 + \frac{1}{4} \right) \right] \|\mathbf{H}\|_\Omega^2 \\
& + \left[\varepsilon_\infty \varepsilon_0^2 \omega_p^2 - \frac{1}{2} \Delta t \varepsilon_0 \omega_p^2 - \frac{C \Delta t \varepsilon_0 \omega_p^2}{h} \left(2 + \frac{1}{4} \right) \right] \|\mathbf{E}\|_\Omega^2 \\
& + \left[1 - \frac{1}{2} \Delta t \varepsilon_0 \omega_p^2 - \frac{C \Delta t \beta^2}{h} \left(2 + \frac{1}{4} \right) \right] \|\mathbf{J}\|_\Omega^2 \\
& + \left[1 - \frac{C \Delta t}{h} \left(2 + \frac{1}{4} \right) \right] \|Q\|_\Omega^2. \qquad (122)
\end{aligned}$$

Thus, the discrete energy will be positive definite if all the coefficients in front of the $\|\cdot\|_\Omega$ terms are positive. Inspired by this argument, we introduce a stability criterion for the time step Δt in the time stepping scheme proposed above.

Proposition 3 *(Positivity of the energy)*

The energy defined by (109) is positive under the following condition

$$\frac{\Delta t}{4h} \leq \min \left\{ \frac{1}{9 \omega_p^2 \varepsilon_0 C}, \frac{\varepsilon_0 \varepsilon_\infty}{2h + 9C}, \frac{1}{2h \varepsilon_0 \omega_p^2 + 9 \beta^2 C}, \frac{1}{9C} \right\}, \qquad (123)$$

where C is a generic constant independent of Δt and h.

Proposition 3 is commonly known as a CFL type criterion.

5 Numerical results

This section is dedicated to numerical results. Beginning with a validation test case in order to guarantee the correct implementation of the numerical scheme (104), the computational results of an infinitely long wire are given in a second part. Subsection 2.8 has already discussed this geometry in an analytical manner. Some of the previous aspects are retrieved in the numerical results. Appendix B provides some supplementary numerical results for further setups of infinitely long 2d examples.

5.1 Implementation

The DGTD method for the non-local dispersion model presented previously has been implemented in a 2d setting for the TE Maxwell equations. From now on, we will use the notation DGTD-$\mathcal{P}_p$ for used basis functions of the polynomial degree p. Due to the second order accuracy of the leap-frog time integration scheme, numerical simulations have been limited to $p \leq 2$. All routines were implemented in Fortran without putting a special effort into performance aspects. The implementation does not provide any parallelization. Although HPC aspects might be of high importance due to the strong β dependency of the CFL criteria, it is not as crucial in 2d as it would be in 3d. Several test cases have been used in the scope of this work. As a test of the spatial discretization and the functionality of the algorithm, we want to compute the field solutions in a cavity that is artificially filled with dispersive metal. After having verified the algorithm's functionality, we stepped further to more applied and physical test cases.

5.2 Dispersive cavity

As a first test case, we want to consider a cavity that is completely filled with dispersive material. Although this is a rather unrealistic test case, it is a simple possibility to test the basic functionalities of the code. The main purpose of this test case is to eliminate as many possible error sources as possible. Of course, analytical solutions for some physically more reasonable geometries exist. For example, the nanodisk, previously discussed in subsection 2.8, would be possible. However, this would require open boundaries and thus many other possible error sources.

5.2.1 Analytical background

Our test case is inspired by [41] and combines the analytical solutions of the electromagnetic and hydrodynamic quantities of a vacuum filled and fully-dispersive cavity,

respectively. In order to compensate the actual coupling of both equations, an artificial test current density is introduced. This current density is computed with the analytical solution of the unperturbed equations (124) and (127). In a first step, the analytical solutions of the homogenous systems are required. The boundary value for Maxwell's equations thus reads

$$\nabla \times \mathbf{E} + \mu_0 \partial_t \mathbf{H} = 0, \tag{124a}$$

$$\nabla \times \mathbf{H} - \varepsilon_0 \partial_t \mathbf{E} = 0, \tag{124b}$$

on the square domain $\Omega_\square = \{(x, y) \in [0, a] \times [0, a]\}$ with the PEC boundary condition

$$\mathbf{n}_{\Omega_\square} \times \mathbf{E} = 0 \quad \text{on } \partial\Omega_\square \times \mathbb{R}^+, \tag{125}$$

for $a > 0$ given. Switching into the frequency domain and retransforming the complex solution gives the electric and magnetic field solution

$$E_x^a(x, y, t) = \frac{x_m}{x_t} \cos(x_m x) \sin(x_m y) \cos(x_t t), \tag{126a}$$

$$E_y^a(x, y, t) = -\frac{x_m}{x_t} \sin(x_m x) \cos(x_m y) \cos(x_t t), \tag{126b}$$

$$H_z^a(x, y, t) = \cos(x_m x) \cos(x_m y) \sin(x_t t). \tag{126c}$$

Here, $x_m = \frac{\pi}{a}$ is the wave number for a square cavity of side length a, which is deduced from the PEC boundary condition. As we are only considering the $\mathrm{TE}_{1,1}$ mode, the signal frequency is given by $f_\square = \frac{c_0}{a\sqrt{2}}$, where c_0 is the speed of light. Subsequently, the angular frequency of the time evolution is determined by $x_t = \frac{\pi\sqrt{2}}{a}$. Analogously to the electrodynamic case, we can define a homogenous hydrodynamic problem that is essentially a wave equation. The reduced problem reads

$$\beta^2 \nabla Q - \partial_t \mathbf{J} = 0, \tag{127a}$$

$$\nabla \cdot \mathbf{J} - \partial_t Q = 0, \tag{127b}$$

on the same domain $\Omega_\square$ (but *filled* with β) and the boundary conditions

$$\mathbf{n}_{\Omega_\square} \cdot \mathbf{J} = 0, \quad \text{on } \in \partial\Omega_\square \times \mathbb{R}^+, \tag{128}$$

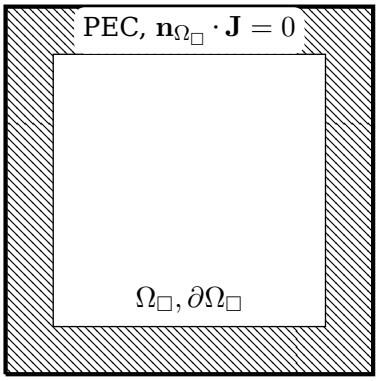

Figure 8: Boundary value problem for the artificial test case. $\Omega_\square$ is either filled with vacuum for the electromagnetic equations or with dispersive material for the hydrodynamic part.

that make exciting currents impossible. The derivation is similar to the one above and leads in time domain to

$$J_x^a(x,y,t) = \beta^2 \frac{x_m}{x_t} \sin(x_m x)\cos(x_m y)\cos(x_t t), \tag{129a}$$

$$J_y^a(x,y,t) = \beta^2 \frac{x_m}{x_t} \cos(x_m x)\sin(x_m y)\cos(x_t t), \tag{129b}$$

$$Q^a(x,y,t) = \cos(x_m x)\cos(x_m y)\sin(x_t t). \tag{129c}$$

Figure 8 illustrates the spatial domain $\Omega_\square$. The superscript a is introduced in order to distinguish the numerical and analytical solution on $[0,a] \times [0,a]$. The resulting formulation of the test case then reads

$$\nabla \times \mathbf{E} + \mu_0 \partial_t \mathbf{H} = 0, \tag{130a}$$

$$\nabla \times \mathbf{H} - \varepsilon_0 \partial_t \mathbf{E} = \mathbf{J} - \mathbf{J}^a, \tag{130b}$$

$$\beta^2 \nabla Q - \partial_t \mathbf{J} = \gamma_c \mathbf{J} - \varepsilon_0 \omega_p^2 \mathbf{E} - \gamma_c \mathbf{J}^a + \varepsilon_0 \omega_p^2 \mathbf{E}^a, \tag{130c}$$

$$\nabla \cdot \mathbf{J} - \partial_t Q = 0. \tag{130d}$$

In the discrete case, the analytical solutions have to be evaluated at the time level corresponding to the time stepping scheme according to Appendix A.2.

5.2.2 Numerical results

As the actual computational results are rather unphysical, we want to focus on the convergence behavior of the algorithm. Defining an error norm $\|\mathbf{E} - \mathbf{E}^a\|_\Omega^2$ on the

domain Ω by

$$\|\mathbf{E}-\mathbf{E}^a\|_\Omega^2 := \sum_{i\in\mathcal{N}_\Omega} \|\mathbf{E}_i-\mathbf{E}^a\|^2_{\mathcal{L}^2(\Omega_i)}, \tag{131}$$

allows the evaluation of an error between the numerically computed and analytical solution. Here, $\mathcal{N}_\Omega$ denotes the partition of Ω in cells Ω_i, and $\mathbf{E}_i$ the numerical solution. The shape of the mesh is sketched in Figure 10 where h is the shortest size of a triangle. Figure 9 illustrates the convergence behavior and for the runs corresponding to Table 2. These results confirm that we have a scheme of order 1 for $\mathcal{P}_1$ and an order 2 scheme for $\mathcal{P}_2$, that corresponds to usual rates of convergence obtained for DGTD schemes based on a centered flux.

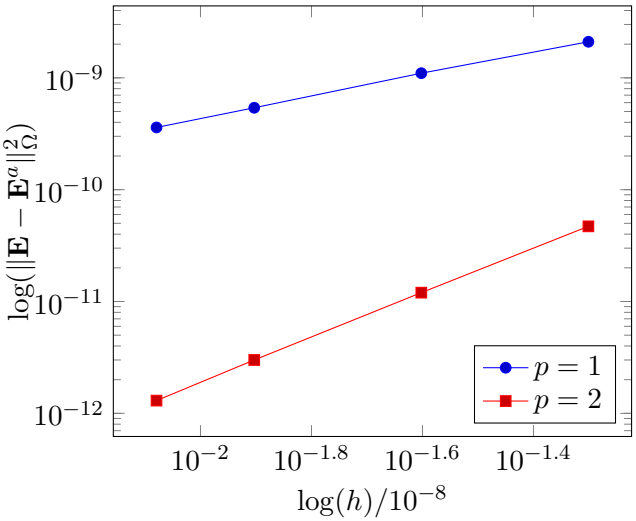

Figure 9: $\mathcal{L}^2(\Omega)$-error for DGTD-$\mathcal{P}_1$ and DGTD-$\mathcal{P}_2$. The convergence rate is 1 and 2 for DGTD-$\mathcal{P}_1$ and DGTD-$\mathcal{P}_2$, respectively. Higher polynomial grades are reasonable since a second order time integration scheme is used. The convergence order can be obtained by $p = \frac{\log(h_2)/\log(h_1)}{\log(\|\mathbf{E}-\mathbf{E}^a\|_\Omega^{h_1})/\log(\|\mathbf{E}-\mathbf{E}^a\|_\Omega^{h_2})}$. Here, h_1 and h_2 are two values for h with $h_2 \neq h_1$.

Table 2: Simulation Parameters for the artificial test cavity. Here, a denotes the length of the cubic domain $\Omega_\square$, h the mesh size according to Figure 10, f the frequency of the $\mathrm{TE}_{1,1}$ mode, and λ the corresponding wavelength. The used time integration scheme was of second order.

$a/$ nm	$h/$ nm	$f/$ PHz	$\lambda/$ nm
10	$0.1, 0.05, 0.025, 0.0125, 0.008\overline{3}$	21.21	14.1

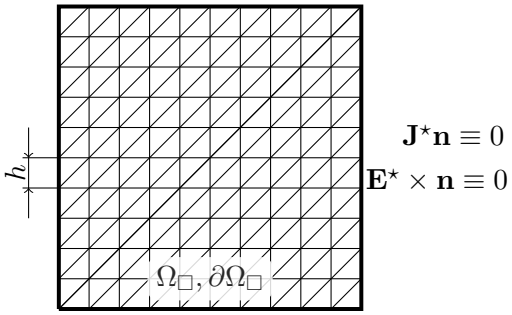

Figure 10: Mesh and boundary conditions for the discrete boundary value problem of the artificial test case. The boundary conditions are imposed via the numerical fluxes of the electric field $\mathbf{E}$ and the current density $\mathbf{J}$ at the boundary $\partial\Omega_\square$.

5.3 Nanodisk

Now, we want to discuss the computation of an infinitely long wire, i.e. a nanodisk. We have chosen this example in order to compare our results in time domain with the FDTD solutions given in [21]. In a first step, a numerical discussion on precision and computational time with respect to the interpolation degree p is given. Physical aspects like the excitation of surface and bulk plasmons are discussed afterwards. In order to guarantee the same experimental setup, we have taken the physical parameters and excitation frequencies from [21] that are summarized in Table 3. A sinusoidal modulated gaussian pulse is used for illumination by means of a plane wave. The temporal modulation is determined by

$$\{\mathbf{E}_{inc}(t), \mathbf{H}_{inc}(t)\} \propto \sin(\omega_c(t-\tau)) \exp\left(-\left(\frac{t-\tau}{\alpha}\right)^2\right), \tag{132}$$

for an incident TE wave that is linearly polarized in x and z direction for $\mathbf{E}$ and $\mathbf{H}$, respectively. The illumination is consequently oriented in $-\mathbf{e}_y$. Table 4 shows the chosen parameters for the excitation signal for the runs with ω_c below and above the plasma frequency. We have used a triangular mesh generator, namely Gmsh. Figure 11 shows the resulting mesh while all runs for $\mathcal{P}_1$ and $\mathcal{P}_2$ use the same mesh. It is very important to provide a sufficiently small mesh size in the dispersive regime due to the small wavelength of the bulk plasmons. As a rule of thumb, we suggest to take a 100 times smaller mesh than for the non dispersive case. On the boundary of the domain, we apply an absorbing boundary condition and the incident field is orthogonally induced from above. For switching from the local to the non-local model, the parameter β is set from 0 to the value given in Table 3. The relative permitivity ε_∞ is set to 1 everywhere.

In the following part, numerical aspects of the implemented DGTD-$\mathcal{P}_p$ method with $p \in \{1, 2\}$ are discussed. Within this work we will limit those aspects to visual

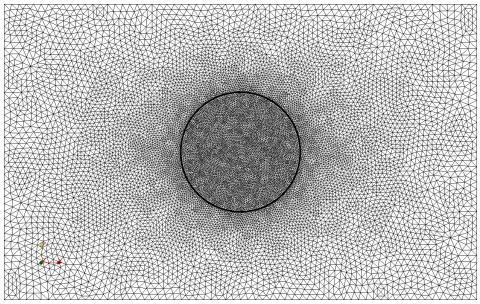

Figure 11: Triangular mesh for a $2\ nm$ dispersive nano disk. The dispersive regime requires a very strong refinement with respect to the usual mesh size for Maxwell's equations. This is mainly caused by the comparatively short wavelength of the bulk plasmon. The total amount of mesh cells counts 6338 triangles.

effects that can be seen in a 2d plot of the computed fields. Nevertheless, it would be of high interest to compare the numerical solutions with Mie theory.

As a figure of merit, we will use the absolute value of the discrete Fourier transform (on the fly) of the computed field quantities. Visualizing the transformed fields at the frequencies $\omega_{c,1}$ and $\omega_{c,2}$ allows a comparison with frequency domain solutions. Figure 12 shows the results for a polynomial degree of $\mathcal{P}_1$ and $\mathcal{P}_2$. Our solutions show a good visual agreement with the mode patterns published in [21] for the DGTD-$\mathcal{P}_2$ run while the solution for DGTD-$\mathcal{P}_1$ is rather blurry. A mesh refinement would improve the quality of the DGTD-$\mathcal{P}_1$ solution. A computation with the grid in Figure 11 together with a total integration time of $5 \cdot 10^{-15}$ s takes about 2 min with the DGTD-$\mathcal{P}_1$ method. Increasing the polynomial order to 2 leads to a computational time of around 10 min. As our code is designed for the non-local model, local Drude solution can be obtained by setting $\beta = 0$. Thus, computations for the local and non-local cases show the same computational time. It may be mentioned that the implementation is neither optimized nor parallized. This will be done for the 3d case in a future work. However, the gain in accuracy for DGTD-$\mathcal{P}_2$ is obvious even for a rather coarse mesh compared to the wavelength of the bulk plasmon.

However, the gain in accuracy for DGTD-$\mathcal{P}_2$ is obvious even for a rather coarse mesh compared to the wavelength of the bulk plasmon. Further, possible improvements are PML boundary conditions [42] or curvilinear elements [43].

Table 3: Physical parameters for the hydrodynamic model. ω_c^1 and ω_c^2 are the two central frequencies of the excitation signal.

ω_p	γ_c	β	$\omega_{c,1}/\omega_p$	$\omega_{c,2}/\omega_p$
$13.39 \cdot 10^{15}$ rad/s	$0.1143 \cdot 10^{15}$ rad/s	$1.1349 \cdot 10^{6}$ m/s	0.6503	1.1963

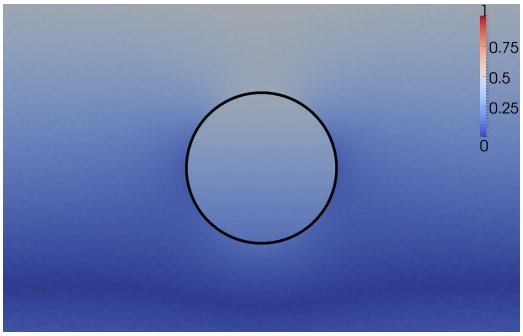

(a) Fourier transformed field plot of $|E_x|$ computed with DGTD-$\mathcal{P}_1$ for the local Drude model. The surface plasmon mode is observable. Also, the mode can penetrate into the dispersive regime because $\omega_{c,2}$ is higher than the plasma frequency.

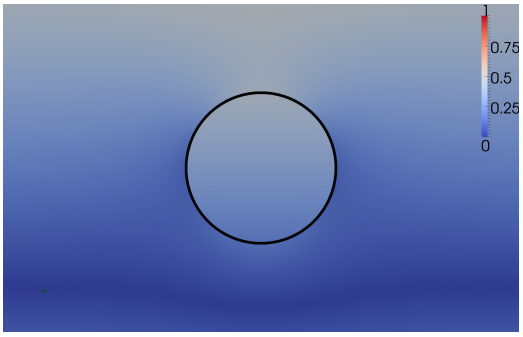

(b) Fourier transformed field plot of $|E_x|$ computed with DGTD-$\mathcal{P}_2$ for the local Drude model. The solution is slightly smoother compared to DGTD-$\mathcal{P}_1$. However, the gain in accuracy is not too obvious.

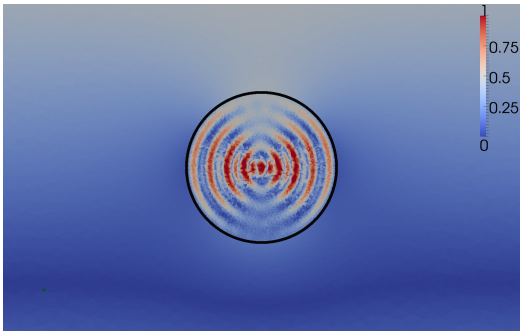

(c) Fourier transformed field plot of $|E_x|$ computed with DGTD-$\mathcal{P}_1$ for the non-local dispersion model. The fourth resonance of the bulk plasmon mode is observable.

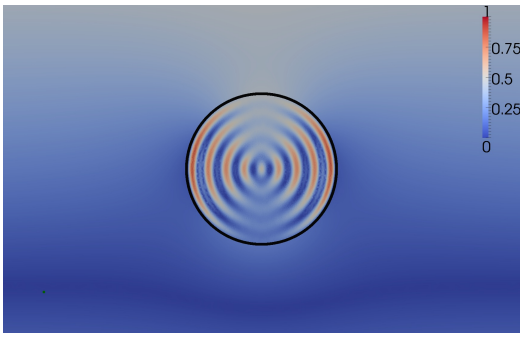

(d) Fourier transformed field plot of $|E_x|$ computed with DGTD-$\mathcal{P}_2$ for the non-local dispersion model. The solution in the dispersive regime is significantly smoother and the maximum amplitude is reduced by factor 2.5.

Figure 12: Field solutions of a dispersive nanodisk with a radius of $2\ nm$. The plots show the Fourier transformed time domain solution of $|E_x|$ for the local and non-local dispersion model with. All computations were done for $\omega_{c,2} = 1.1963\omega_p$ for DGTD-$\mathcal{P}_1$ and DGTD-$\mathcal{P}_2$, respectively.

Table 4: Simulation parameters of the illuminating field for the runs below and above the plasma frequency. Here, the subscript i links α_i to the computational run with $\omega_{c,i}$, for $i = 1, 2$.

T_{max}	α_1	α_2	τ_1	τ_2
$5 \cdot 10^{-15}$ s	$2 \cdot 10^{16}$ s	$1 \cdot 10^{-16}$ s	$1 \cdot 10^{-17}$ s	$1 \cdot 10^{-17}$ s

5.3.1 Physical discussion

After having discussed the numerical framework, its limits and its validation, we now want to have a look on the physical interpretation of the computed results. The following computations were all done with the DGTD-$\mathcal{P}_2$ method and the same parameters as above. We basically compare the results for the local Drude model with the non-local hydrodynamic model. For the angular frequency $\omega_{c,1}$, we would expect small differences between both models. As this frequency is below the plasma frequency, only surface plasmons can be excited. Figure 13 shows the Fourier transformed field solutions for the E_x and E_y component. Both field patterns have more or less the same shape. However, the local model allows a very small penetration that is almost not visualizable. In contrast, the non-local solution makes penetration easier and we can see the strongest penetration in the direction of the incident field polarization. This is fairly reasonable since the plasmon gets excited due to the electric field. In other words, the electrons get *pushed* by the incident field. We want to emphasize that the shown field distributions correspond to the absolute value of the discrete Fourier transform. What seems to be a quadrupole field is in reality a dipole field.

Let us switch to the second angular frequency $\omega_{c,2}$ that is clearly above the plasma frequency and corresponds to the fifth bulk plasmon resonance according to the cross-section calculations in [21]. Figure 14 shows the obtained field plots. Again, the local Drude model excites a surface plasmon. This plasmon has a lower amplitude as for $\omega_{c,1}$. Since $\omega_{c,1}$ was exactly chosen to be at the resonance peak, this is not surprising. For the non-local model however, we can see a completely different field pattern. The surface plasmon is still slightly observable but the solution is dominated by the bulk plasmon. Analogously to the result below the plasma frequency, the excited bulk plasmon reaches the highest amplitudes where the surface normal is tangential to the incident field. As a last remarkable result, we want to have a look at the scattered field due to the excited resonances. The probable most appropriate way to study the resonance behavior of a nanostructure might be the evaluation of the cross section. Since this has not been implemented in the code yet, it is still possible to observe the time evolution of the electromagnetic field at a determined point in the computational domain. In our case, the field monitor was placed at the point $(x, y) = (0\ \mathrm{m}, 4.5 \cdot 10^{-10}\ \mathrm{m})$ for the E_x component of the electric field. Figure 15 shows the observed results. The blueshift of the surface plasmonic

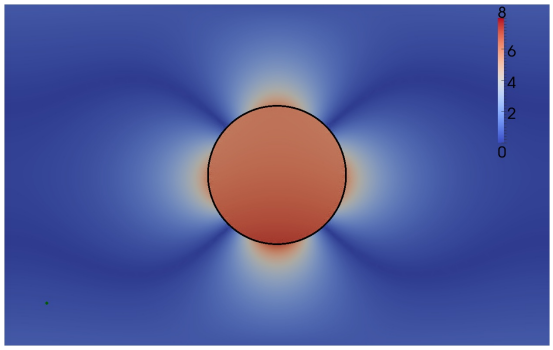

(a) $|E_x|$ for the local Drude model. The surface plasmon mode is clearly observable. Although the local model allows a penetration, it is hardly seeable due to the very short penetration depth.

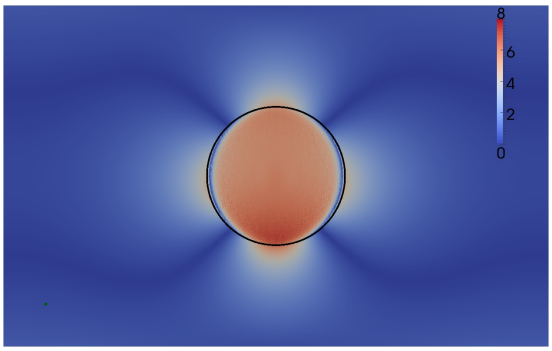

(b) $|E_x|$ for the non-local dispersion model. The surface plasmon mode is clearly observable. Due to the electron interaction of the non-local model, the surface plasmon is able to penetrate the surface easier than for the local model.

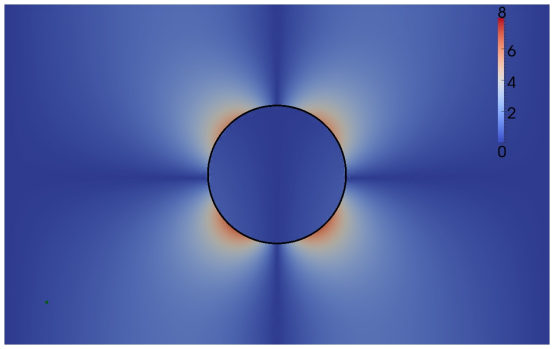

(c) $|E_y|$ for the local Drude model. The surface plasmon mode is clearly observable. Although the local model allows a penetration, it is hardly seeable due to the very short penetration depth.

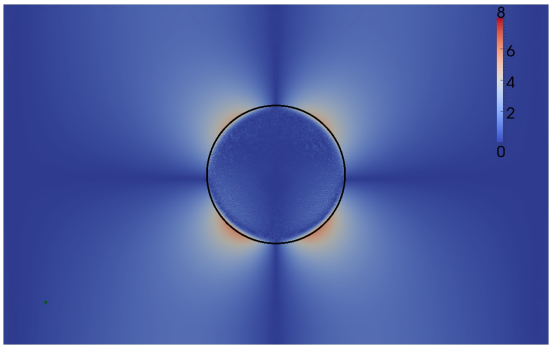

(d) $|E_y|$ for the non-local dispersion model. The surface plasmon mode is clearly observable. Due to the electron interaction of the non-local model, the surface plasmon is able to penetrate the surface easier than for the local model.

Figure 13: Field solutions of a dispersive nanodisk with a radius of 2 nm. The four figures show the Fourier transformed field solutions of $|E_x|$ and $|E_y|$ for the local and non-local dispersion model. All computations were done with DGTD-$\mathcal{P}_2$ at $\omega_{c,1}$.

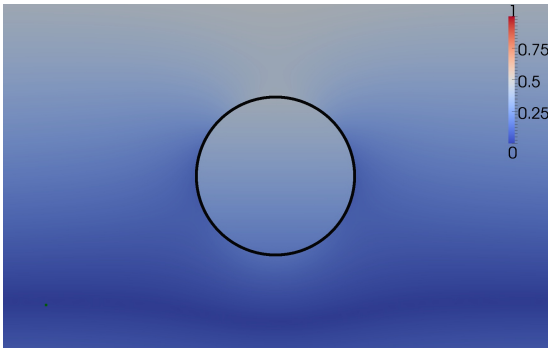

(a) $|E_x|$ for the local Drude model. The surface plasmon mode is still observable although the amplitude has reduced by a factor of 16. Since the frequency is now higher than the plasma frequency ω_p, penetration is possible.

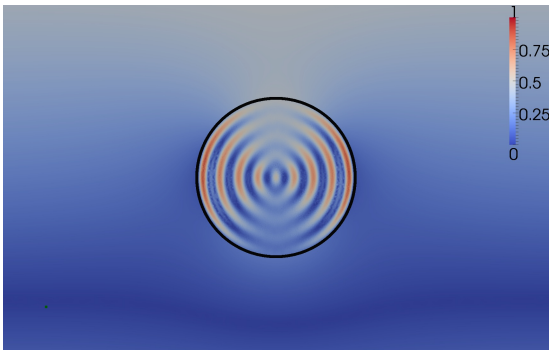

(b) $|E_x|$ for the non-local dispersion model. Due to nonlocality, bulk plasmons are excited that penetrate into the inner of the disk. Here, we can clearly see the fifth order resonance.

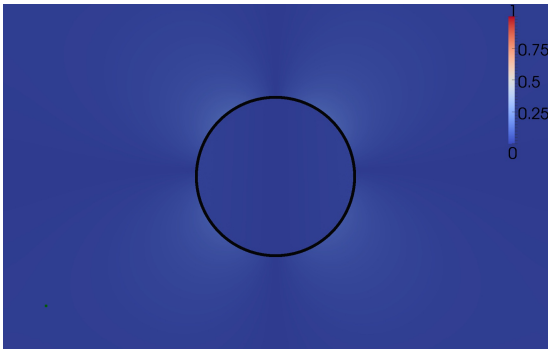

(c) $|E_y|$ for the local Drude model. Similarly to the E_x component, the maximum field intensity is reduced with respect to the the illumination with $\omega_{c,1}$. Since the frequency is now higher than the plasma frequency ω_p, penetration is possible.

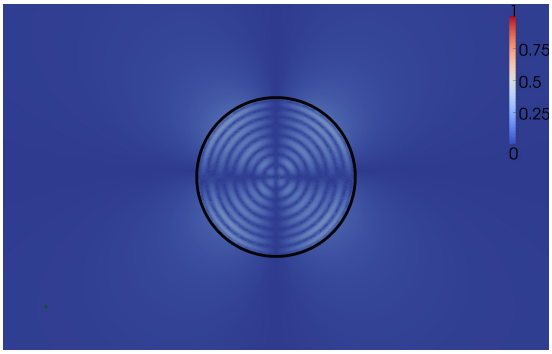

(d) $|E_y|$ for the non-local dispersion model. Due to nonlocality, bulk plasmons are excited that penetrate into the inner of the disk.

Figure 14: Field solutions of a dispersive nanodisk with a radius of 2 nm. The four figures show the Fourier transformed field solutions of $|E_x|$ and $|E_y|$ for the local and non-local dispersion model. All computations were done with DGTD-$\mathcal{P}_2$ at $\omega_{c,2}$.

response for the non-local model is clearly observable and thus agrees with discussions in [33] and [21].

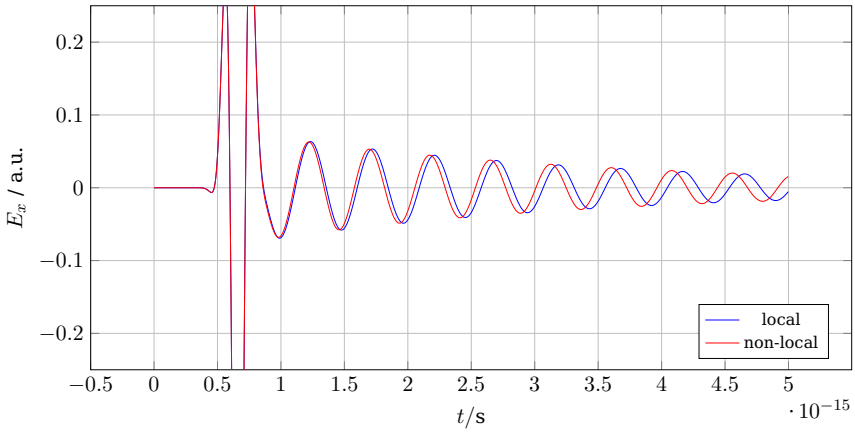

Figure 15: E_x component of the electric field at the point $(x, y) = (0\ \mathrm{m}, 4.5 \cdot 10^{-10}\ \mathrm{m})$. The excitation signal is almost zero after $t = 1 \cdot 10^{-15}$ s and only the emitted field due to the excited plasmon can be observed. A blue shift of the resonance frequency w.r.t. the local model can be observed for the non-local model.

6 Conclusions

We have studied a non-local dispersion model in the context of nanophotonics. The considered dispersion law is a linearized version of a non-linear hydrodynamic modeling of the electron gas for metals. As a matter of fact, the resulting coupled problem of Maxwell's equations together with the non-local dispersion model is still hyperbolic and the total energy is bounded.

The spatial discretization of the coupled system with the DG method led to a stable semi-discrete scheme. Discretizing this semi-discrete scheme in time with a second order leap-frog scheme, finally led to a fully-discrete formulation. Due to the explicit time integration scheme, a stability criterion was derived. This criterion was given as a CFL type criterion.

In order to verify our 2d implementation, we first considered a rather unphysical test case that allowed a verification of the spatial discretization. After having successfully tested the implementation, we considered an infinitely long nanowire. The computed time domain solutions were Fourier transformed and compared to frequency domain solutions afterwards. Our results show a good agreement with earlier published articles.

With this code, a time domain solver for the linearized hydrodynamic model is available now. One of the main advantages is the possibility to illuminate with arbitrarily shaped signals. Although frequency domain solvers are generally able to

treat arbitrarily time signals, the computational costs increase dramatically for very short pulses and thus time domain algorithms are more appropriate.This allows new insights into the behavior of nano particles. Future works could extend this work in many directions. For example, more sophisticated electron gas models, e.g. non-linear hydrodynamic approaches that govern SHG or even higher order harmonic generation are possible. Also, from a more numerical point of view, a 3d implementation, curvilinear elements, parallelization and higher order time integration schemes are natural paths for furture works.

Acknowledgment. Many thanks to Prof. Dr.-Ing. Thomas Weiland and Dr.-Ing. Wolfgang Ackermann for the fruitful discussions about the results of this work.

Appendix

A Discontinuous Galerkin method

A.1 Semi-conservation law formulation

The DGM will be applied to the hydrodynamic model. Differently to the previous formulation system (33) is written in a multidimensional conservative form.

$$\mathbf{f}(\mathbf{u}) := \begin{pmatrix} \mathbf{f}_x & \mathbf{f}_y & \mathbf{f}_z \end{pmatrix}, \tag{133}$$

$$\mathbf{f}_i = \mathbb{N}_i \cdot \mathbf{u}, \tag{134}$$

$$\mathbf{u} := \begin{pmatrix} E_x & \dots & H_x & \dots & J_x & \dots & Q \end{pmatrix}^T, \tag{135}$$

where $\mathbb{N}_i$ are the matrices that represent the topological curl , div and, grad of system (33). Hence, (33) can be generally expressed as

$$\partial_t \mathbb{L}\mathbf{u} + \nabla \cdot \mathbf{f}(\mathbf{u}) = \mathbb{B}\mathbf{u}, \tag{136}$$

where

$$\nabla \cdot \mathbf{f}(\mathbf{u}) = \partial_x \mathbf{f}_x + \partial_y \mathbf{f}_y + \partial_z \mathbf{f}_z \tag{137}$$

$$= \mathbb{N}_x \partial_x \mathbf{u}_x + \mathbb{N}_y \partial_y \mathbf{u}_y + \mathbb{N}_z \partial_z \mathbf{u}_z. \tag{138}$$

After having applied the projection to a scalar test function ϕ, the upper system reads

$$\partial_t \int_\Omega \mathbb{L}\mathbf{u}\phi \ \mathrm{d}^3\mathbf{r} + \int_\Omega \nabla \cdot \mathbf{f}(\mathbf{u})\phi \ \mathrm{d}^3\mathbf{r} = \int_\Omega \mathbb{B}\mathbf{u}\phi \ \mathrm{d}^3\mathbf{r}. \tag{139}$$

With $\nabla\cdot(\phi\mathbf{A}) = \phi\nabla\cdot\mathbf{A} + \mathbf{A}\cdot\nabla\phi$ and sufficient regularity for ϕ. This yields

$$\partial_t \int_\Omega \mathbb{L}\mathbf{u}\phi \ \mathrm{d}^3\mathbf{r} + \int_{\partial\Omega_\Omega} \phi\mathbf{f}^\star(\mathbf{u})\cdot\mathbf{n} \ \mathrm{d}^2\mathbf{r} - \int_\Omega \mathbf{f}(\mathbf{u})\cdot\nabla\phi \ \mathrm{d}^3\mathbf{r} = \int_\Omega \mathbb{B}\mathbf{u}\phi \ \mathrm{d}^3\mathbf{r}, \tag{140}$$

where the matrices $\mathbb{L}$ and $\mathbb{B}$ contain the material properties. The mass matrix for the first term on the left hand side is now derived. Let us first define two new vectors and recall the dimensions

$$\mathbb{L},\mathbb{B} \in \mathbb{R}^{10\times 10}, \tag{141}$$

$$\bar{\mathbf{u}} := \begin{pmatrix} \sum_{j=1}^{P_i} e_{ip}^x\phi_{ip} & \dots & \sum_{j=1}^{P_i} q_{ip}\phi_{ip} \end{pmatrix}^T, \quad \in \mathbb{R}^{10\times 1} \tag{142}$$

$$\tilde{\mathbf{u}} := \begin{pmatrix} e_{i1}^x & \dots & q_{iP} \end{pmatrix}, \quad \in \mathbb{R}^{10\cdot P\times 1}. \tag{143}$$

Now, the mass matrix is derived by inserting the approximation from a finite functional space $\bar{\mathbf{u}}$

$$\int_{\Omega_i} \mathbb{L}\mathbf{u}\phi_{ik} \ \mathrm{d}^3\mathbf{r} \xrightarrow{\sim} \int_{\Omega_i} \mathbb{L}\bar{\mathbf{u}}\phi_{ik} \ \mathrm{d}^3\mathbf{r}, \tag{144}$$

and thus for each element Ω_i

$$\int_{\Omega_i} \mathbb{L}\bar{\mathbf{u}}\phi_{ik} \ \mathrm{d}^3\mathbf{r} \Rightarrow \mathbb{M}^i\tilde{\mathbf{u}}_i, \tag{145}$$

$$\left(\left(\mathbb{M}_{\mathbb{L}}^i\right)_l\right)_{kj} := \int_{\Omega_i} \alpha_l\phi_{ij}\phi_{ik}, \quad l \in x,y,z \tag{146}$$

$$\mathbb{M}_{\mathbb{L}}^i = \begin{pmatrix} \begin{pmatrix} \mathbb{M}_{\alpha_1} & & \\ & \mathbb{M}_{\alpha_2} & \\ & & \mathbb{M}_{\alpha_3} \end{pmatrix} & & \\ & \ddots & \\ & & \ddots \end{pmatrix}. \tag{147}$$

This steps are performed analogously for $\mathbb{B}$. For the stiffness term

$$\int_{\Omega_i} \mathbf{f}(\mathbf{u}) \cdot \nabla \phi_{ik} \, \mathrm{d}^3\mathbf{r} \xrightarrow{\sim} \int_{\Omega_i} \left[\mathbb{N}_x \bar{\mathbf{u}}_i \partial_x \phi_{ik} + \mathbb{N}_y \bar{\mathbf{u}}_i \partial_y \phi_{ik} + \mathbb{N}_z \bar{\mathbf{u}}_i \partial_z \phi_{ik} \right] \, \mathrm{d}^3\mathbf{r}, \tag{148}$$

$$\int_{\Omega_i} \mathbb{N}_a \bar{\mathbf{u}}_i \partial_a \phi_{ik} \, \mathrm{d}^3\mathbf{r} = \mathbb{N}_a \int_{\Omega_i} \bar{\mathbf{u}}_i \partial_a \phi_{ik} \, \mathrm{d}^3\mathbf{r} \Rightarrow \tilde{\mathbb{N}} \mathbb{S}_i^a \tilde{\mathbf{u}}_i, \tag{149}$$

$$\left((\mathbb{S}_i^a)_l \right)_{kj} := \int_{\Omega_i} \phi_{ij} \partial_a \phi_{ij} \, \mathrm{d}^3\mathbf{r}, \tag{150}$$

$$\mathbb{S}_i^a = \mathrm{diag} \left((\mathbb{S}_i^a)_{E_x} \dots (\mathbb{S}_i^a)_q \right), \tag{151}$$

$$\mathbb{S}_i = \tilde{\mathbb{N}}_x \mathbb{S}_i^x + \tilde{\mathbb{N}}_y \mathbb{S}_i^y + \tilde{\mathbb{N}}_z \mathbb{S}_i^z, \tag{152}$$

where $\tilde{\mathbb{N}}_a$ is $\mathbb{N}_a$ 'stretched' by $I \in \mathbb{R}^{P \times P}$. For the flux we get

$$\int_{\partial\Omega_i} \phi_{ik} \mathbf{f}^\star(\mathbf{u}) \cdot \mathbf{n} \, \mathrm{d}^2\mathbf{r} = \int_{\partial\Omega_i} \phi_{ik} \left[\mathbf{f}_x^\star(\mathbf{u}) n_x + \mathbf{f}_y^\star(\mathbf{u}) n_y + \mathbf{f}_z^\star(\mathbf{u}) n_z \right] \, \mathrm{d}^2\mathbf{r}, \tag{153}$$

with a central scheme

$$\mathbf{f}_a^\star|_{s_{iq}} := \frac{\mathbf{f}_{a,i} + \mathbf{f}_{a,q}}{2}, a \in \{x, y, z\}. \tag{154}$$

Thus, the surface integral reads

$$\int_{\partial\Omega_i} \phi_{ik} \mathbf{f}_a^\star(\mathbf{u}) \, \mathrm{d}^2\mathbf{r} = \sum_{q=1}^{N_q} \int_{s_{iq}} \phi_{ik} \frac{\mathbf{f}_{a,i} + \mathbf{f}_{a,q}}{2} n_{iq}^a \, \mathrm{d}^2\mathbf{r}, \tag{155}$$

$$= \frac{1}{2} \sum_{q=1}^{N_q^i} \int_{s_{iq}} \phi_{ik} \left(\mathbb{N}_a \bar{\mathbf{u}}_i + \mathbb{N}_a \bar{\mathbf{u}}_q \right) n_{iq}^a \, \mathrm{d}^2\mathbf{r}, \tag{156}$$

$$= \underbrace{\frac{1}{2} \sum_{q=1}^{N_q^i} \int_{s_{iq}} \phi_{ik} \mathbb{N}_a \bar{\mathbf{u}}_i n_{iq}^a \, \mathrm{d}^2\mathbf{r}}_{\text{self flux}} + \underbrace{\frac{1}{2} \sum_{q=1}^{N_q^i} \int_{s_{iq}} \phi_{ik} \mathbb{N}_a \bar{\mathbf{u}}_q n_{iq}^a \, \mathrm{d}^2\mathbf{r}}_{\text{neighbor flux}}. \tag{157}$$

We get for the self flux

$$\left(\left({}^{a}_{s}\mathbb{F}_i\right)_l\right)_{kj} := \frac{1}{2}\sum_{q=1}^{N_q^i}\int_{s_{iq}} \phi_{ik}\phi_{ij}n^a_{iq}\,\mathrm{d}^2\mathbf{r}, \tag{158}$$

$$\tilde{\mathbb{N}}_a\ \left({}^{a}_{s}\mathbb{F}_i\right)\tilde{\mathbf{u}}_i, \tag{159}$$

$${}^{a}_{s}\mathbb{F}_i = \mathrm{diag}\left\{\left({}^{a}_{s}\mathbb{F}_i\right)_{E_x}\dots\left({}^{a}_{s}\mathbb{F}_i\right)_q\right\}, \tag{160}$$

and for the neighbor flux

$$\left(\left({}^{a}_{s}\mathbb{F}^q_i\right)_l\right)_{kj} := \frac{1}{2}\int_{s_{iq}} \phi_{ik}\phi_{qj}n^a_{iq}\,\mathrm{d}^2\mathbf{r}, \tag{161}$$

$$\Rightarrow \sum_{q=1}^{N_q^i}\tilde{\mathbb{N}}_a\left({}^{a}_{s}\mathbb{F}^q_i\right)\tilde{\mathbf{u}}_q. \tag{162}$$

The *external* flux matrices are *off-diagonal* and their position in the system matrix depends on the grid (they have to be multiplied with the corresponding $\mathbf{u}_q$ parts of the $\mathbf{u}$ vector that contains all DoFs. Adding up the flux matrices $\mathbb{F} = \mathbb{F}_x + \mathbb{F}_y + \mathbb{F}_z$ to one general flux matrix allows to write the total system with mimetic operators in the form of

$$\mathbb{M}_{\mathbb{L}}\partial_t\tilde{\mathbf{u}} = \left(\mathbb{S} - \mathbb{F} + \mathbb{M}_{\mathbb{B}}\right)\tilde{\mathbf{u}}, \tag{163}$$

or equivalently

$$\partial_t\tilde{\mathbf{u}} = \mathbb{M}_{\mathbb{L}}^{-1}\left(\mathbb{S} - \mathbb{F} + \mathbb{M}_{\mathbb{B}}\right)\tilde{\mathbf{u}}. \tag{164}$$

However, this formulation is equivalent to section 3.2 in the linear case. The advantage of this formulation becomes clear when a time integration scheme is applied to (164). Since this formulation is obviously of the form

$$\partial_t\mathbf{x} = \mathbf{f}(\mathbf{x}, t), \tag{165}$$

any time integration scheme for ODE can be generally applied. Of course, it obliges to the schemes' designer to guarantee stability and convergence.

A.2 Semi-discrete formulation for normalized fields

Considering system (73) for all cells simultaneously in one complete system of ODE gives

$$\mathbb{S}\mathbf{h} + \mathbb{F}_{\mathsf{curl}}\,\mathbf{h} = \varepsilon_0\varepsilon_\infty \partial_t \mathbb{M}\mathbf{e} + \mathbb{M}\mathbf{j}, \tag{166a}$$

$$\mathbb{S}\mathbf{e} + \mathbb{F}_{\mathsf{curl}}\,\mathbf{e} = -\mu_0 \partial_t \mathbb{M}\mathbf{h}, \tag{166b}$$

$$-\mathbb{G}\mathbf{q} + \mathbb{F}_{\mathsf{grad}}\,\mathbf{q} = \frac{1}{\beta^2}\partial_t \mathbb{M}\mathbf{j} + \frac{\gamma}{\beta}\mathbb{M}\mathbf{j} - \frac{\varepsilon_0\omega_p^2}{\beta^2}\mathbb{M}\mathbf{e}, \tag{166c}$$

$$-\mathbb{D}\mathbf{j} + \mathbb{F}_{\mathsf{div}}\,\mathbf{j} = \partial_t \mathbf{q}, \tag{166d}$$

where the vectors of the DoFs $\mathbf{a} \in \{\mathbf{h}, \mathbf{e}, \mathbf{j}, \mathbf{q}\}$ contain the DoFs of all cells. The matrices $\mathbb{M}$, $\mathbb{S}, \mathbb{G}, \mathbb{D}$, and $\mathbb{F}_{\mathsf{curl}}$, $\mathbb{F}_{\mathsf{grad}}$, $\mathbb{F}_{\mathsf{div}}$ are build in accordance to subsections 3.3, 3.4, and 3.5, respectively. If we now take into account the normalization as presented in section 2.9, the upper system reads

$$\mathbb{S}\tilde{\mathbf{h}} + \mathbb{F}_{\mathsf{curl}}\,\tilde{\mathbf{h}} = \tilde{\varepsilon}_\infty \partial_{\tilde{t}} \mathbb{M}\tilde{\mathbf{e}} + \mathbb{M}\tilde{\mathbf{j}}, \tag{167a}$$

$$\mathbb{S}\tilde{\mathbf{e}} + \mathbb{F}_{\mathsf{curl}}\,\tilde{\mathbf{e}} = -\partial_{\tilde{t}} \mathbb{M}\tilde{\mathbf{h}}, \tag{167b}$$

$$-\mathbb{G}\tilde{\mathbf{q}} + \mathbb{F}_{\mathsf{grad}}\,\tilde{\mathbf{q}} = \frac{1}{\tilde{\beta}^2}\partial_{\tilde{t}} \mathbb{M}\tilde{\mathbf{j}} + \frac{\tilde{\gamma}}{\tilde{\beta}^2}\mathbb{M}\tilde{\mathbf{j}} - \frac{\tilde{\omega_p^2}}{\tilde{\beta}^2}\mathbb{M}\tilde{\mathbf{e}}, \tag{167c}$$

$$-\mathbb{D}\tilde{\mathbf{j}} + \mathbb{F}_{\mathsf{div}}\,\tilde{\mathbf{j}} = \partial_{\tilde{t}} \mathbb{M}\tilde{\mathbf{q}}. \tag{167d}$$

A.3 Fully-discrete formulation for normalized fields

Using the second order leap-frog scheme for the time integration finally gives the following update equations

$$\mathbf{e}^{n+1} = \mathbf{e}^n + \frac{\Delta t}{\varepsilon_\infty}\mathbf{j}^{n+\frac{1}{2}} + \frac{\Delta t}{\varepsilon_\infty}\mathbb{M}^{-1}\left[\mathbb{S}\mathbf{h}^{n+\frac{1}{2}} + \mathbb{F}_{\mathsf{curl}}\,\mathbf{h}^{n+\frac{1}{2}}\right], \tag{168a}$$

$$\mathbf{h}^{n+\frac{3}{2}} = \mathbf{h}^{n+\frac{1}{2}} - \Delta t \mathbb{M}^{-1}\left[\mathbb{S}\mathbf{e}^{n+1} + \mathbb{F}_{\mathsf{curl}}\,\mathbf{h}^{n+1}\right], \tag{168b}$$

$$\mathbf{q}^{n+1} = \mathbf{q}^{n+1} + \Delta t \mathbb{M}^{-1}\left[-\mathbb{G}\mathbf{j}^{n+\frac{1}{2}} + \mathbb{F}_{\mathsf{grad}}\,\mathbf{h}^{n+1}\right], \tag{168c}$$

$$\begin{aligned}\mathbf{j}^{n+\frac{3}{2}} = {} & \frac{2-\gamma\Delta t}{2+\gamma\Delta t}\mathbf{j}^{n+\frac{1}{2}} + \frac{2\omega_p^2\Delta t}{2+\gamma\Delta t}\mathbf{e}^{n+1} \\ & + \frac{2\beta^2\Delta t}{(2+\gamma\Delta t)}\mathbb{M}^{-1}\left[-\mathbb{G}\mathbf{q}^{n+1} + \mathbb{F}\mathbf{q}^{n+1}\right].\end{aligned} \tag{168d}$$

Here, we disregarded the tilde over each quantity.

B Additional numerical examples

Some additional computational results are presented in the following. The first example is an infinitely long nanowire that is rectangularly shaped. Subsequently, two nanodisks that are sufficiently narrowly placed in order to allow some mutual coupling were computed with two different distances. The last presented geometry are two mutually coupled rectangles, similar to the precedent case with two nanodisks. All computations were done with the same setup as in section 5.3 at $\omega_c = \omega_{c,2}$.

B.1 Rectangular nanowire

For the rectangular nanowire, an edge length of $l = 4\ nm$ is chosen. Analogously to section 5.3, the illumination is still from above with all the parameters. The resulting Fourier transformed field patterns are illustrated in Figure 16 for the $|E_x|$ and $|E_y|$ component of the electric field.

Since the illuminating field does only have an electric field component in $\mathbf{e}_x$ direction, bulk plasmons are mainly excited in the same direction. The interesting pattern of $|E_y|$ is a bit surprising to us since we rather expected a vanishing electric field in $\mathbf{e}_y$ direction. A possible explanation could be the retarded excitation of the bulk plasmon w.r.t. the incident direction of the illumination. This causes a bulk plasmon wave front that is not parallel to the square edges and thus causes a gradient in $\mathbf{e}_y$ direction of the charge density Q. Having a look at the system (33) explains the excitation of $\mathbf{e}_y$ polarized electrical fields due to the ∇Q. Interfering waves in the middle of the square could explain the E_y at the edges.

In any case, an increase of the physical simulation time smoothens out the Fourier transformed solutions due to a longer (in time) Fourier transformation.

B.2 Coupled nanodisks

Bringing two nanodisks closely together should allow some mutual coupling of the disks. We can indeed observe this effect by placing two identical disks of the same size as in section 5.3 with a center distance of $d_{\text{disks},1} = 4.6\ \text{nm}$ and in a second run of $d_{\text{disks},2} = 4.2\ \text{nm}$. Regarding to the discussions in chapter 2, those results have to be taken with care. Since we have reduced the distance between the surfaces of our nano obstacles below $1\ nm$, QM effects may be taken into account. Nevertheless, it is nice to see how the mutual coupling affects the characteristics of two particles in terms of the frequency response. Figure 17 shows the Fourier transformed field pattern of two nanodisks with the distance $d_{\text{disks},1}$. The mode pattern of each individual disk is slightly asymmetric with respect to Figure 14. Once the disks get even closer, see Figure 19, this effect increases. The coupled disks behave more and more as one nano particle of a bigger size and experience a resonance shift similar to the one shown in Figure 15, see Figure 18.

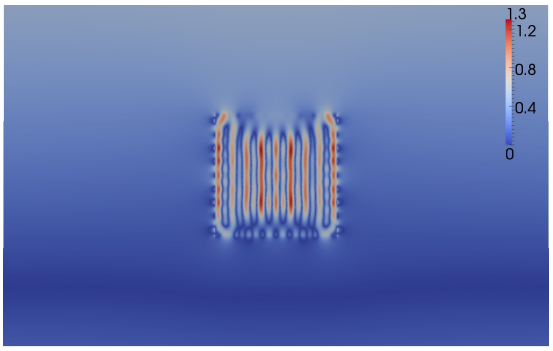

(a) Fourier transformed solution of $|E_x|$ computed with DGTD-$\mathcal{P}_2$ for a nanosquare. Since the illuminating electrical field is polarized in $\mathbf{e}_x$ direction, the excited bulk plasmon is mainly excited in $\mathbf{e}_x$ direction as well. The finite simulation time causes the varying patern in $\mathbf{e}_x$ direction for in the Fourier transformed solution.

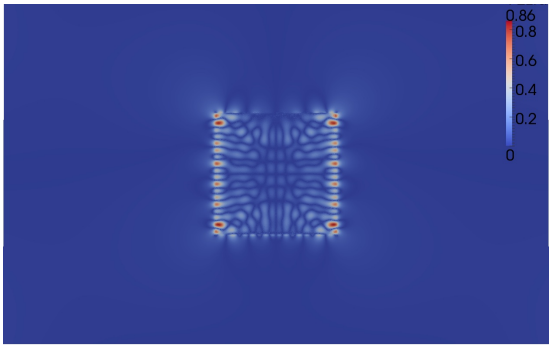

(b) Fourier transformed solution of $|E_y|$ computed with DGTD-$\mathcal{P}_2$ for a nanosquare. The electrical field in $\mathbf{e}_y$ is probably excited because of the retarded excited bulk plasmon (see main text).

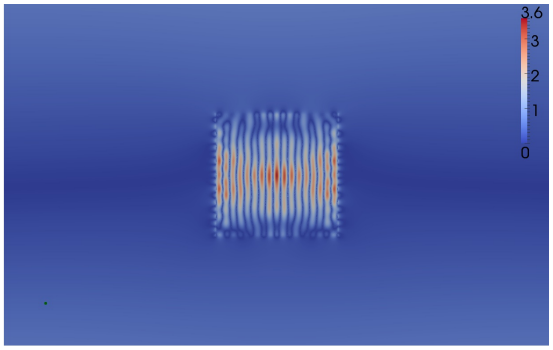

(c) Fourier transformed solution of $|E_x|$ computed with DGTD-$\mathcal{P}_2$ for a nanosquare. Here, the computation time is two times longer compared to Figure 16a which leads to a smoother pattern.

(d) Fourier transformed solution of $|E_y|$ computed with DGTD-$\mathcal{P}_2$ for a nanosquare. Here, the computation time is two times longer compared to Figure 16b which leads to a smoother pattern.

Figure 16: Electric field pattern for a nanosquare. The upper plots show the Fourier transformed time domain solution for a total simulation time $T_{max} = 5 \cdot 10^{-15}$ s while the lower plot's run took lasted $T_{max} = 10 \cdot 10^{-15}$ ns. All computations were performed with DGTD-$\mathcal{P}_2$ at $\omega_{c,2}$.

A careful look to the signal time evolution of the E_x signal in Figure 18 gives rise to the assumption that the coupled system has more than one strong resonance. Thus, the coupled nanodisks have their individual mode plus a contributing coupled mode with a lower frequency, observable as a beat on E_x.

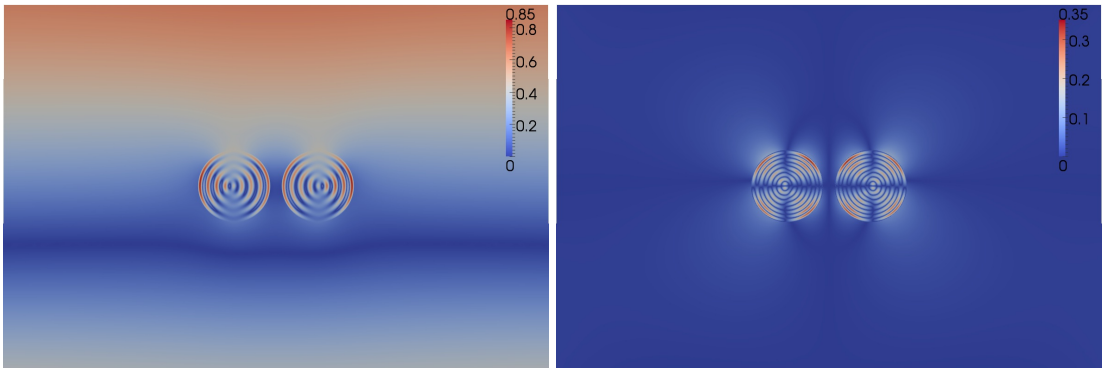

(a) $|E_x|$ for the non-local dispersion model. The mutual coupling causes an asymmetric mode pattern compared to the single disk pattern.

(b) $|E_y|$ for the non-local dispersion model. The mutual coupling causes an asymmetric mode pattern compared to the single disk pattern.

Figure 17: Field solutions of two dispersive nanodisks with a radius of $2\ nm$. The distance between both centers measures $d^1_{disk} = 4.6\ nm$. Each individual disk shows a small asymmetric mode pattern compared to the single disk case. All computations were done with DGTD-$\mathcal{P}_2$ at $\omega_{c,2}$.

References

[1] A. Moreau, C. Ciraci, D. Smith, Impact of nonlocal response on metallodielectric multilayers and optical patch antennas, Phys. Rev. B 87 (045401-1–045401-11) (2013) 6795–6820.

[2] T. Lu, W. Cai, P. Zhang, Discontinuous Galerkin methods for dispersive media and lossy Maxwell's equations and PML boundary conditions, J. Comp. Phys. 200 (2004) 549–580.

[3] J. Niegemann, R. Diehl, K. Busch, Efficient low-storage Runge-Kutta schemes with optimized stability regions, J. Comput. Phys. 231 (2) (2012) 364–372.

[4] X. Ji, W. Cai, P. Zhang, High-order DGTD method for dispersive Maxwell's equations and modelling of silver nanowire coupling, Int. J. Numer. Meth. Engng. 69 (2007) 308–325.

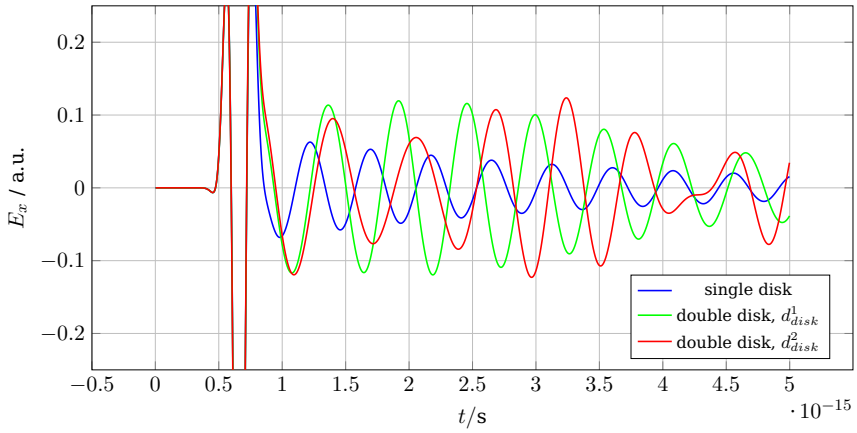

Figure 18: E_x component of the electric field at the point $(x, y) = (0\ \mathrm{m}, 4.5 \cdot 10^{-10}\ \mathrm{m})$. The excitation signal is almost zero after $t = 1 \cdot 10^{-15}$ s and only the emitted field due to the excited plasmon can be observed. A red shift of the resonance frequency for the coupled nanodisks can be observed. This red shift increases for a smaller distance. Additionally, a beat occurs probable because the coupling allows more resonances. (The beat is more obvious for longer simulations.)

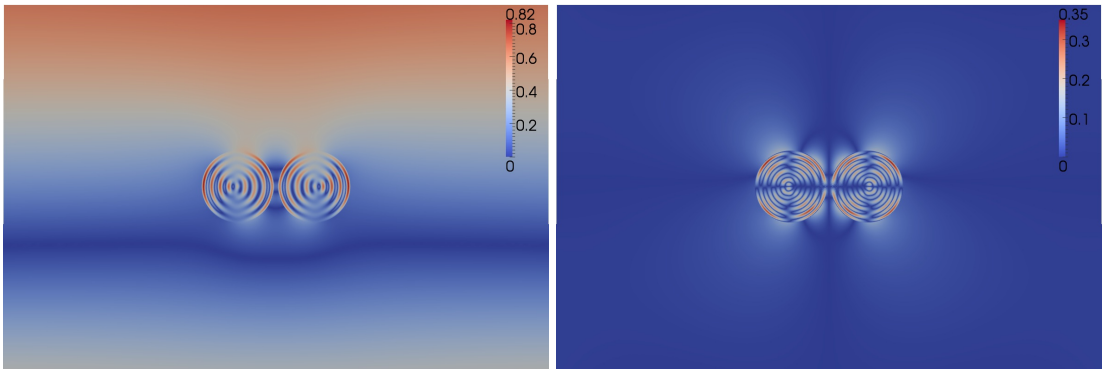

(a) $|E_x|$ for the non-local dispersion model. The asymmetry increases due to the shorter distance between both disks that yields to a higher mutual coupling.

(b) $|E_x|$ for the non-local dispersion model. The asymmetry increases due to the shorter distance between both disks that yields to a higher mutual coupling.

Figure 19: Field solutions of two dispersive nanodisks with a radius of 2 nm. The distance between both centers measures $d^1_{disk} = 4.2\ nm$. Each individual disk shows a small asymmetric mode pattern compared to the single disk case. All computations were done with DGTD-$\mathcal{P}_2$ at $\omega_{c,2}$.

[5] S. Gedney, J. Young, T. Kramer, J. Roden, A discontinuous Galerkin finite element time-domain method modeling of dispersive media, IEEE Trans. Antennas and Propag. 60 (4) (2012) 1969–1977.

[6] J. Li, Y. Chen, V. Elander, Mathematical and numerical study of wave propagation in negative-index material, Comput. Meth. App. Mech. Engng. 197 (2008) 3976–3987.

[7] J. Li, Numerical convergence and physical fidelity analysis for Maxwell's equations in metamaterials, Comput. Methods. Appl. Mech. Engrg. 198 (2009) 3161–3172.

[8] L. Fezoui, S. Lanteri, S. Lohrengel, S. Piperno, Convergence and stability of a discontinuous Galerkin time-domain method for the 3D heterogeneous Maxwell equations on unstructured meshes, ESAIM: Math. Model. Numer. Anal. 39 (6) (2005) 1149–1176.

[9] J. Viquerat, S. Lanteri, C. Scheid, Theoretical and numerical analysis of local dispersion models coupled to a discontinuous galerkin time-domain method for Maxwell's equations, Tech. Rep. RR-8298, INRIA (2013).

[10] J. Jackson, Classical electrodynamics, John Wiley & Sons, 1999.

[11] C. Kittel, Einführung in die Festkörperphysik, 14. Auflage (German), Oldenburg, 2006.

[12] G. Sotiriou, F. Starsich, A. Dasargyri, M. Wurnig, F. Krumeich, A. Boss, J.-C. Leroux, S. Pratsinis, Photothermal killing of cancer cells by the controlled plasmonic coupling of silica-coated Au/Fe2O3 nanoaggregates, Adv. Funct. Mater. 24 (19) (2014) 2818–2827.

[13] I. Larkin, M. I. Stockmann, Imperfect perfect lens, Nano Lett 5 (2005) 339–343.

[14] R. Yang, Z. Lu, Subwavelength plasmonic waveguides and plasmonic materials, Intern. J. Opt.

[15] Y. Chen, H. Ming, Review of surface plasmon resonance and localized surface plasmon resonance sensor, Photonic Sensors 2 (1) (2012) 37–49.

[16] M. Stockmann, Nanoplasmonics: the physics behind the applications, Physics Today 2014 64 (2) (2011) 39–44.

[17] T. Teperik, P. Nordlander, J. Aizpurua, A. Borisos, Quantum plamonics: nonlocal effects in coupled nanowire dimer, Optics Express 21 (22) (2013) 27306–27325.

[18] G. Toscano, S. Raza, A.-P. Jauho, N. Mortensen, M. Wubs, Modified field enhancement in plasmonic nanowire dimers due to nonlocal response, Optics Express 20 (4) (2011) 4176–4188.

[19] S. Maier, Plasmonics - Fundamentals and applications, Springer, 2007.

[20] P. Johnson, R. Christy, Optical constants of the noble metals, Physical Review B 6 (1972) 4370–4379.

[21] S. Raza, G. Toscano, A.-P. Jauho, M. Wubs, N. Mortensen, Unusual resonances in nanoplasmonic structures due to nonlocal response, Phys. Rev. B 84 (121412) (2011) 1–4.

[22] R. Esteban, A. Borisov, P. Nordlander, Bridging quantum and classical plasmonics with a quantum-corrected model, Nature Communications 3 (825) (2012) 1–9.

[23] F. Chen, Introduction to plasma physics and controlled fusion: plasma physics, Springer, 2006.

[24] C. David, N. Mortensen, J. Christensen, Perfect imaging, epsilon-near zero phenomena and waveguiding in the scope of nonlocal effects, Scientific Reports 3 (2526) (2013) 1–7.

[25] N. Mortensen, Nonlocal formalism for nanoplasmonics: phenomenological and semi-classical considerations, Photonics and Nanostructures - Fundamentals and Applications 11 (4) (2013) 303–309.

[26] A. Boardman, Electromagnetic surface modes, John Wiley & Sons, 1972.

[27] K. Hiremath, L. Zschiedrich, F. Schmidt, Numerical solution of nonlocal hydrodynamic Drude model for arbritrary shaped nano-plasmonic structures using Nedelec finite elements, J. Comput. Phys. 231 (2012) 5890–5896.

[28] S. Benzoni-Gavage, D. Serre, Multi-dimensional hyperbolic partial differential equations. First-order systems and applications, Oxford Mathematical Monographs, 2006.

[29] G. Barton, Some surface effects in the hydrodynamic model of metals, Rep. Prog. Phys. 42 (6) (1979) 963.

[30] J. Pitarke, V. Silkin, E. Chulkov, P. Echenique, Theory of surface plasmons and surface-plasmon polaritons, Rep. Prog. Phys. 70 (1) (2007) 963.

[31] R. Ruppin, Optical properties of a spatially dispersive cylinder, J. Opt. Soc. Am. 6 (8) (1989) 1559–1563.

[32] J. McMahon, , S. Gray., G. Schatz, Nonlocal optical response of metal nanostructures with arbitrary shape, Phys. Rev. Lett. 103 (9) (2009) 097403.

[33] T. Christensen, W. Yan, S. Raza, A.-P. Jauho, N. Mortensen, M. Wubs, Nonlocal response of metallic nanopheres probed by light, electrons and atoms, ACS Nano 8 (2) (2014) 1745—-1758.

[34] W. Reed, T. Hill, Triangular mesh methods for the neutron transport equation, Tech. Rep. 479, Los Alamos Scientific Laboratory (1973).

[35] J. Hesthaven, T. Warburton, Nodal discontinuous Galerkin methods: algorithms, analysis and applications, Springer Texts in Applied Mathematics, Springer Verlag, 2007.

[36] H. Fahs, Development of a hp-like discontinuous Galerkin time-domain method on non-conforming simplicial meshes for electromagnetic wave propagation, Int. J. Numer. Anal. Model. 6 (2) (2009) 193–216.

[37] H. Fahs, S. Lanteri, A high-order non-conforming discontinuous Galerkin method for time-domain electromagnetics, J. Comp. Appl. Math. 234 (2010) 1088–1096.

[38] S. Schnepp, Space-time adaptive methods for beam dynamic simulations, Ph.D. thesis, Technische Universität Darmstadt, Germany (2009).

[39] K. Yee, Numerical solution of initial boundary value problems involving Maxwell's equations in isotropic media, IEEE Trans. Antennas and Propag. 14 (3) (1966) 302–307.

[40] S. Brenner, R. Scott, The mathematical theory of finite element methods, Springer, 2008.

[41] C. Scheid, S. Lanteri, Convergence of a discontinuous Galerkin scheme for the mixed time domain Maxwell's equations in dispersive media, IMA J. Numer. Anal. 33 (2) (2013) 432–459.

[42] J. Niegemann, M. König, K. Stannigel, K. Busch, Higher-order time-domain methods for the analysis of nano-photonic systems, Photonics Nanostruct. - Fundamentals and Applications 7 (2009) 2–11.

[43] T. Warburton, A low storage curvilinear discontinuous Galerkin time-domain method for electromagnetics, in: 2010 URSI International Symposium on Electromagnetic Theory (EMTS), IEEE Xplore, Berlin, 2010, pp. 996–999.

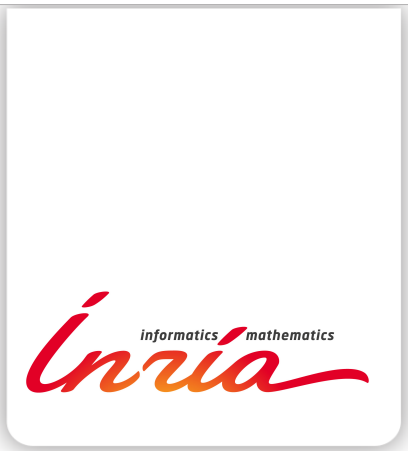

RESEARCH CENTRE
SOPHIA ANTIPOLIS – MÉDITERRANÉE

2004 route des Lucioles - BP 93

06902 Sophia Antipolis Cedex

Publisher
Inria
Domaine de Voluceau - Rocquencourt
BP 105 - 78153 Le Chesnay Cedex
inria.fr

ISSN 0249-6399